Diboson production in the SMEFT at dimension-8

Hesham El Faham, a,b,c Giuseppe Ventura, a Eleni Vryonidou a,d

- ^aDepartment of Physics and Astronomy, University of Manchester, Oxford Road, Manchester M13 9PL, United Kingdom
- ^bTIFLab, Università degli Studi di Milano, Via Celoria 16, 20133 Milano, Italy
- ^cINFN, Sezione di Milano, Via Celoria 16, 20133 Milano, Italy

ABSTRACT: We present a comprehensive analysis of dimension-8 and dimension-6 effects in fully leptonic WZ and WW production at the Large Hadron Collider (LHC) within the Standard Model (SM) Effective Field Theory (SMEFT). We focus on dimension-8 operators with maximal energy growth in the quark–(anti)quark-initiated production channel and assess their impact differentially through a variety of observables, including polarisation-sensitive ones. Leveraging existing data from measurements at the LHC, we perform fits to quantify the sensitivity of current and future data to dimension-8 effects and evaluate their interplay with squared dimension-6 contributions. By marginalising over the dimension-8 operators we examine the robustness of a dimension-6 SMEFT analysis in diboson production. We find that dimension-8 effects become subdominant only for new-physics scales above 3 TeV.

Keywords: SMEFT, diboson, dimension-8 operators

^dDepartment of Physics, University of Cyprus, P.O. Box 20537, 1678 Nicosia, Cyprus E-mail: hesham.elfaham@unimi.it, giuseppe.ventura@manchester.ac.uk, vryonidou.eleni@ucy.ac.cy

Co	ontents			
1	Introduction	1		
2	Theoretical framework	3		
3	Computational setup	6		
4	Results	7		
	4.1 Differential distributions	8		
	4.2 Polarisation fractions	14		
5	Sensitivity study	17		
	5.1 Fit method and results	18		
	5.2 Impact of dimension-8 operators in the fit	19		
	5.3 Two-dimensional scans	21		
6	Conclusions	24		
\mathbf{A}	A Additional results			

1 Introduction

In the absence of direct evidence for new resonances or states, the LHC has transitioned into an era of precision searches for new physics, leveraging highly precise differential measurements to indirectly probe deviations from the Standard Model (SM). The Standard Model Effective Field Theory (SMEFT) provides a systematic, model-agnostic framework for characterising these potential deviations via higher-dimensional operators modifying SM interactions.

Electroweak (EW) diboson production stands out as a particularly promising channel to search for new physics (NP) effects. In the fully leptonic final states, $W^{\pm}Z$ and $W^{+}W^{-}$ —hereafter referred to as WZ and WW—production channels offer clean experimental signatures and direct sensitivity to triple gauge couplings (TGCs). The ATLAS and CMS collaborations have performed detailed studies of the WZ channel, examining both polarisation states and spin correlations [1–3], benefiting from high signal purity and the ability to fully reconstruct the final state up to a single neutrino. The anticipated large datasets from Run 3 and the High-Luminosity LHC (HL-LHC) will significantly enhance the precision achievable in differential measurements of these processes and extend the kinematic range of the corresponding observables.

On the theory side, SM predictions have matured substantially, incorporating next-to-next-to-leading order (NNLO) QCD [4, 5] and next-to-leading order (NLO) EW corrections [6–9], along with advanced parton-shower (PS) matching and resummation techniques [10–18]. Predictions for intermediate polarised bosons in the pole [19–22] or narrow-width approximation [23–25] are also known up to (N)NLO in QCD [26–28] and NLO EW [29–32] accuracy, including also NLO matching to PS [33, 34].

The WZ channel has been extensively studied. At leading order, the process is exclusively qq—initiated, whereas NLO order QCD contributions also involve $q(\bar{q})g$ channels. It is well established [9, 35] that in the SM, the NLO QCD corrections are substantial, predominantly due to hard real-emission configurations, particularly those where a high- p_T electroweak boson recoils against a jet and a softer boson, and the large gluon parton luminosity. The NLO electroweak corrections to the WZ fully leptonic final state are moderate—few percent [8, 9]—but become increasingly negative at high transverse momenta because of sizeable virtual EW Sudakov logarithms [36, 37].

The combination of precise theory predictions and of precise highly differential measurements render diboson production a great testing ground for EFT analyses. As such, a plethora of SMEFT analyses traditionally concentrated on dimension-6 operators [38–59], have explored diboson production. SMEFT analyses of diboson production have explored how to resurrect the typically suppressed interference effects from the dimension-6 triple gauge coupling operator [42, 43, 48, 60]. Recently, Ref. [61] has emphasised that a linear EFT interpretation of diboson measurements is casting doubts on the validity of the EFT for weakly coupled UV scenarios. Due to these observations and the particular nature of the diboson process, compelling arguments motivate extending the exploration also to dimension-8 operators. Notably, dimension-8 operators introduce novel Lorentz and gauge structures that are absent at dimension-6, such as the neutral triple gauge coupling (nTGC)—see, for example, Ref. [62]. Additionally, at $\mathcal{O}(\Lambda^{-4})$, dimension-8 contributions naturally appear alongside the squared dimension-6 ones, making their inclusion, a priori, essential for a consistent EFT expansion. Motivated by these arguments, several studies have appeared in the literature exploring higher dimension effects in diboson production [54, 63-67]. Whilst these studies focus on the quark initiated channel, a recent study investigated dimension-8 effects in diboson production, focusing on gluon-initiated WW production [68], and concluded that the impact of dimension-8 SMEFT contributions is negligible.

In this work, we aim to establish, in a model independent manner, the size of the dimension-8 contributions and to determine whether these contributions can significantly influence the constraints set on the dimension-6 triple gauge interactions and thus invalidate the EFT interpretation of diboson measurements within the dimension-6 SMEFT. We focus on a set of dimension-8 operators that induce energy-growing contributions scaling as s^2/Λ^4 in quark–(anti)quark-initiated—referred to as qq-initiated—diboson production as classified in Ref. [54].

We present a comprehensive analysis of dimension-8 SMEFT effects in WZ and WW production at the LHC at $\sqrt{s} = 13$ TeV. Our analysis examines a broad spectrum of differential and angular observables, including polarisation-sensitive distributions, within both

an inclusive and an experimentally realistic fiducial setups. We also examine the angular coefficients, ones which are directly related to the polarisation fractions, and investigate possible contributions from the SMEFT at both the dimension-6 and dimension-8 levels. Furthermore, we perform fits to existing LHC measurements as well as HL-LHC projections to assess the sensitivity of current and future data to dimension-8 effects, investigating the interplay between linear dimension-8 and quadratic dimension-6 contributions.

This paper is structured as follows: Sections 2 and 3 outline our theoretical framework and computational methods, respectively. Our predictions and results for WZ and WW production are presented and discussed in Section 4, and a sensitivity study based on current measurements and HL-LHC projections is showcased in Section 5. We summarise our findings in Section 6.

2 Theoretical framework

We study diboson, VV, production at the LHC, incorporating dimension-6 and dimension-8 SMEFT modifications. A typical SMEFT expansion takes the form:

$$\mathcal{L}_{EFT} = \mathcal{L}_{SM} + \sum_{i} \frac{C_i^{(6)} \mathcal{O}_i^{(6)}}{\Lambda^2} + \sum_{j} \frac{C_j^{(8)} \mathcal{O}_j^{(8)}}{\Lambda^4} + \mathcal{O}(\Lambda^{-6}).$$
 (2.1)

In physical observables the squared contributions of dimension-6 operators scale as $\mathcal{O}(\Lambda^{-4})$, and thus appear at the same order as the linear contributions from dimension-8 operators. Our aim is to assess the phenomenological impact of the latter in comparison to the former.

Dimension-6 SMEFT operators have been systematically classified, most notably in the so-called Warsaw basis [69]. Bases for dimension-8 operators have also been constructed [70, 71] and a generalisation of the basis construction at any mass dimension has been achieved [72–74]. A key challenge at this order lies in the sheer number of independent operators that can be constructed [70, 71]: whilst dimension-8 terms allow for richer Lorentz and gauge structures than their dimension-6 counterparts, they do so at the cost of introducing a significantly larger operator basis. We will now discuss the operators we consider in this work.

Dimension-6 we focus on the modifications to the TGCs induced by the CP-even, \mathcal{O}_W , and CP-odd, $\mathcal{O}_{\widetilde{W}}$, dimension-6 operators:

$$\epsilon_{ijk}W^i_{\mu\nu}W^{j,\nu\rho}W^{k,\mu}_{\rho}, \qquad \epsilon_{ijk}\tilde{W}^i_{\mu\nu}W^{j,\nu\rho}W^{k,\mu}_{\rho},$$
 (2.2)

where $W_{\mu\nu}$ denotes the dual field strength tensor. Operators modifying $Vq\bar{q}$ interactions also enter in diboson production but these are sufficiently well constrained and thus do not any affect any constraints set on C_W . This result is confirmed by the recent global SMEFT fit in Ref. [75], which finds nearly identical individual and marginalised bounds on the CP-even coefficient C_W , with the full sensitivity driven by diboson production at the LHC. This justifies our choice of considering only the operators of Eq. (2.2) at dimension-6.

In an analysis of recent diboson measurements [57], we have explored how constraints on these operators depend on whether the analysis includes only the linear or both linear

and quadratic contributions. Quadratic bounds are significantly more stringent than the linear ones. This is related to the helicity selection rules which suppress the interference of the dimension-6 operator with the SM. Quadratic dominated bounds often cast doubt on the validity of the EFT and motivates the inclusion of all effects at $\mathcal{O}(\Lambda^{-4})$.

At $\mathcal{O}(\Lambda^{-4})$, one encounters contributions from dimension-8 operators at linear order, the squared terms of dimension-6 operators, as well as their double insertions. In addition to the operators of Eq. (2.2), operators introducing modifications to the $Vq\bar{q}$ couplings are, in principle, contributing—either via double insertions or through the quadratic contributions from single insertions—we have verified that both types of modifications exhibit suppressed energy growth relative to the linear contributions from dimension-8 operators. They are therefore expected to be subdominant. It is worth noting that we refer here to modifications of the $Vq\bar{q}$ vertex induced by current-type SMEFT operators; modifications arising from dipole-type SMEFT operators are suppressed under Minimal Flavour Violation assumptions [76]. Finally, possible deformations in the lepton sector that could enter via EW boson decays are also omitted as they are already tightly constrained by LEP data [75].

In summary, our analysis includes the purely dimension-6 modification arising from \mathcal{O}_W and $\mathcal{O}_{\tilde{W}}$, as well as the maximally growing dimension-8 operators discussed below.

Dimension-8 we make use of the classification of dimension-8 operators relevant to VV production in the SMEFT as presented in Ref. [54] where the authors have listed all dimension-8 operators that generate contact interactions for the qq-initiated production channels of WZ and WW inducing an s^2/Λ^4 enhancement in the amplitude in the high energy regime. These are listed in Table 1. It is worth noting that not all operators listed

$$\begin{array}{lll} \mathcal{O}_{1}=iB^{\mu}{}_{\nu}B^{\nu}{}_{\lambda}(\bar{d}\gamma^{\lambda} \overleftrightarrow{D}_{\mu}d) & \mathcal{O}_{10}=iW^{I\mu}{}_{\nu}W^{I\nu}{}_{\lambda}\left(\bar{q}\gamma^{\lambda} \overleftrightarrow{D}_{\mu}q\right) \\ \mathcal{O}_{2}=iB^{\mu}{}_{\nu}B^{\nu}{}_{\lambda}(\bar{u}\gamma^{\lambda} \overleftrightarrow{D}_{\mu}u) & \mathcal{O}_{11}=i\epsilon^{IJK}W^{I\mu}{}_{\nu}W^{J\nu}{}_{\lambda}\left(\bar{q}^{i}\gamma^{\lambda}\tau_{i}^{Kj} \overleftrightarrow{D}_{\mu}q_{j}\right) \\ \mathcal{O}_{3}=iB^{\mu}{}_{\nu}B^{\nu}{}_{\lambda}\left(\bar{q}\gamma^{\lambda} \overleftrightarrow{D}_{\mu}q\right) & \mathcal{O}_{12}=i\epsilon^{IJK} \tilde{W}^{I\mu}{}_{\nu}W^{J\nu}{}_{\lambda}\left(\bar{q}^{i}\gamma^{\lambda}\tau_{i}^{Kj} \overleftrightarrow{D}_{\mu}q_{j}\right) \\ \mathcal{O}_{4}=iW^{I\mu}{}_{\lambda}B^{\nu\lambda}\left(\bar{q}^{i}\gamma_{\nu}\tau_{i}^{Ij} \overleftrightarrow{D}_{\mu}q_{j}\right) & \mathcal{O}_{13}=i\epsilon^{IJK}W^{I\mu}{}_{\nu}\tilde{W}^{J\nu}{}_{\lambda}\left(\bar{q}^{i}\gamma^{\lambda}\tau_{i}^{Kj} \overleftrightarrow{D}_{\mu}q_{j}\right) \\ \mathcal{O}_{5}=iW^{I\mu}{}_{\lambda}\tilde{B}^{\nu\lambda}\left(\bar{q}^{i}\gamma_{\nu}\tau_{i}^{Ij} \overleftrightarrow{D}_{\mu}q_{j}\right) & \mathcal{O}_{14}=i\left(\bar{u}\gamma^{\lambda} \overleftrightarrow{D}_{\mu}u\right)\left(D_{\lambda}H^{\dagger}D^{\mu}H\right) \\ \mathcal{O}_{6}=iW^{I\nu}{}_{\lambda}B^{\mu\lambda}\left(\bar{q}^{i}\gamma_{\nu}\tau_{i}^{Ij} \overleftrightarrow{D}_{\mu}q_{j}\right) & \mathcal{O}_{15}=i\left(\bar{d}\gamma^{\lambda} \overleftrightarrow{D}_{\mu}d\right)\left(D_{\lambda}H^{\dagger}D^{\mu}H\right) \\ \mathcal{O}_{7}=iW^{I\nu}{}_{\lambda}\tilde{B}^{\mu\lambda}\left(\bar{q}^{i}\gamma_{\nu}\tau_{i}^{Ij} \overleftrightarrow{D}_{\mu}q_{j}\right) & \mathcal{O}_{16}=i\left(\bar{q}\gamma^{\lambda} \overleftrightarrow{D}_{\mu}q\right)\left(D_{\lambda}H^{\dagger}D^{\mu}H\right) \\ \mathcal{O}_{8}=iW^{I\mu}{}_{\nu}W^{I\nu}{}_{\lambda}(\bar{d}\gamma^{\lambda} \overleftrightarrow{D}_{\mu}d) & \mathcal{O}_{17}=i\left(\bar{q}\gamma^{\lambda}\tau^{K} \overleftrightarrow{D}_{\mu}q\right)\left(D_{\lambda}H^{\dagger}\tau^{K}D^{\mu}H\right) \\ \mathcal{O}_{9}=iW^{I\mu}{}_{\nu}W^{I\nu}{}_{\lambda}(\bar{u}\gamma^{\lambda} \overleftrightarrow{D}_{\mu}u) & \mathcal{O}_{18}=i(\bar{u}\gamma^{\mu} \overleftrightarrow{D}^{\nu}d)\epsilon^{ij}(D^{\mu}H_{i}D^{\nu}H_{j}) \end{array}$$

Table 1: List of energy-growing dimension-8 operators contributing to qq-initiated VV production as listed in Ref. [54]. $W^I_{\mu\nu}$ and $B_{\mu\nu}$ are the $SU(2)_L$ and $U(1)_Y$ field-strength tensors, H is the Higgs doublet, q indicates the $SU(2)_L$ symmetric quark doublet, and u and d are the right-handed up and down singlet quark fields, respectively. Generation indices for the quark fields are understood.

there are relevant for the processes considered in this work, namely WZ and WW. In par-

ticular, some operators contribute exclusively to ZZ production and are therefore omitted from our analysis. The subsets of operators relevant to our study are the following:

$$WZ : \{\mathcal{O}_4, \mathcal{O}_5, \mathcal{O}_6, \mathcal{O}_7, \mathcal{O}_{11}, \mathcal{O}_{12}, \mathcal{O}_{13}, \mathcal{O}_{17}, \mathcal{O}_{18}\}, WW : \{\mathcal{O}_8, \mathcal{O}_9, \mathcal{O}_{10}, \mathcal{O}_{11}, \mathcal{O}_{12}, \mathcal{O}_{13}, \mathcal{O}_{14}, \mathcal{O}_{15}, \mathcal{O}_{16}, \mathcal{O}_{17}\},$$

$$(2.3)$$

where only three operators, \mathcal{O}_5 , \mathcal{O}_7 , and \mathcal{O}_{11} , are CP-odd, whilst all others are CP-even.

Among the relatively large number of dimension-8 operators contributing to WZ and WW production via the qq-initiated channel presented in Eq. (2.3), a hierarchy emerges in their energy growth either at the amplitude level or after integration over phase space. For completeness and to motivate our focus on the leading energy-growth effects, we summarise here the key arguments of Ref. [54] regarding the scaling behaviour of the operators in Eq. (2.3). These considerations explain the origin of the hierarchy—both at the amplitude level and following phase-space integration—and justify restricting our analysis to the subset of operators that dominate the energy growth.

WW at dimension-8 since the SM diboson amplitude vanishes for opposite-helicity states, any non-zero interference between the EFT and SM amplitudes requires a helicity flip. Such flips can occur, for example, through insertions of the gauge-boson mass, m_V , which introduce a suppression factor of at least one power of mass. Consequently, the resulting interference amplitude from $\mathcal{O}_{(8,9)}$ grows only as $\sim s$ at high energy. In contrast, the operators $\mathcal{O}_{(14,15)}$ probe the longitudinal modes of the gauge bosons. Owing to their additional derivative structure, their contributions to the amplitude scale as $\sim s^2$ at high energy.

The operator $\mathcal{O}_{(11)}$ is CP-odd, resulting in a vanishing interference with the CP-even SM amplitude for the $2 \to 2$ amplitudes. Interference involving CP-odd operators can re-emerge in $2 \to 4$ amplitudes [42, 48, 52, 54]. However, we find that such contributions are generally negligible in our analysis, particularly in the WW channel, where they are statistically compatible with zero—similar observations have been found in Ref. [57]. For this reason, we do not present CP-odd results for the WW process.

This leaves the operators $\mathcal{O}_{(16,17,10,12,13)}$, which each yield amplitudes scaling as $\sim s^2$ at high energy. However, after the angular phase-space integration, only $\mathcal{O}_{(10,12,13)}$ retain this leading growth. The operators $\mathcal{O}_{(8,9,11,14,15)}$ integrate to zero, whilst $\mathcal{O}_{(16,17)}$ suffer a 1/s suppression. This hierarchy is most transparently understood via the J-basis formalism and partial wave decomposition, as detailed in Ref. [54].

WZ at dimension-8 the operators $\mathcal{O}_{(5,7,11)}$ are CP-odd. However, unlike in the WW case, possible $2 \to 2$ non-interference with the SM can be resurrected by including the finite width effects. The operator $\mathcal{O}_{(18)}$ couples only to right-handed quarks, which also leads to zero interference with the SM. Therefore, the only CP-even operators we need to consider in our study are $\mathcal{O}_{(4,6,12,13)}$.

After accounting for the high-energy scaling of the dimension-8 operators, the relevant subsets in Eq. (2.3) reduce to smaller sets which we consider in this study, namely

$$WZ: \{ \mathcal{O}_4, \mathcal{O}_5, \mathcal{O}_6, \mathcal{O}_7, \mathcal{O}_{11}, \mathcal{O}_{12}, \mathcal{O}_{13} \}, \qquad WW: \{ \mathcal{O}_{10}, \mathcal{O}_{12}, \mathcal{O}_{13} \}.$$
 (2.4)

3 Computational setup

We study the production of WZ and WW at the LHC at $\sqrt{s} = 13 \text{ TeV}$, focusing on fully leptonic final states, namely

$$pp \to e^+ \nu_e \,\mu^+ \mu^-, \qquad pp \to e^+ \nu_e \,\mu^- \bar{\nu}_\mu,$$
 (3.1)

for WZ and WW, respectively. Predictions are obtained at NLO in QCD for the SM and when including the dimension-6 SMEFT operators, \mathcal{O}_W and $\mathcal{O}_{\tilde{W}}$, and at LO in the presence of the dimension-8 operators listed in Eq. (2.4).

The calculations are performed in the G_{μ} scheme [22, 77], which is well-suited for SMEFT analyses in light of recent recommendations from the LHC EFT Working Group [78]. The Fermi constant is set to $G_{\mu} = 1.16638 \cdot 10^{-5} \text{ GeV}^{-2}$. Unstable particles are treated using the complex-mass scheme [79–81]. The masses of the EW gauge bosons are $m_W = 80.379 \text{ GeV}$ and $m_Z = 91.1876 \text{ GeV}$. The top-quark pole mass and width, relevant for bottom-induced WW production, are $m_t = 172 \text{ GeV}$ and $\Gamma_t = 1.47 \text{ GeV}$, respectively.

All computations are performed in the five-flavour scheme. Parton distributions are taken from the NNPDF3.1 NLO set [82] with $\alpha_{\rm s}(m_Z)=0.118$ accessed via the LHAPDF interface [83]. We adopt fixed renormalisation and factorisation scales, in line with recent SM polarisation analyses [26–34], namely

$$\mu_{\rm R} = \mu_{\rm F} = \begin{cases} \frac{m_W + m_Z}{2}, & \text{for } WZ, \\ m_W, & \text{for } WW. \end{cases}$$
(3.2)

It has been shown in Ref. [57] that using a dynamical scale yields results consistent with the fixed-scale choice, both at the inclusive level and for differential observables.

The SM and dimension-6 SMEFT predictions for both processes have been cross-validated against the results in Ref. [57]. SMEFT predictions are obtained using the SMEFT@NLO model [84] implemented in MadGraph5_aMC@NLO [85]. The model has been extended to include the CP-odd triple-gauge operator, $\mathcal{O}_{\tilde{W}}$, relevant for our study. For the dimension-8 results, we generated our UFO model [86] based on the FeynRules [87] implementation of the SMEFT developed in [54]. This UFO model was interfaced with MadGraph5_aMC@NLO to generate parton-level predictions for the relevant processes.

 \mathbf{WZ} we consider both inclusive and fiducial selection criteria for WZ production. The inclusive setup imposes only a single requirement: a mass window on the same-flavour, opposite-sign lepton pair, namely

$$81 \,\text{GeV} < m_{\mu\mu} < 101 \,\text{GeV} \,.$$
 (3.3)

The fiducial selection follows closely the event-level criteria adopted in Refs. [1, 3], and—in addition to the invariant mass window in Eq. (3.3)—is defined as:

$$p_T^e > 20 \,\text{GeV} \,, \qquad p_T^{\mu^{\pm}} > 15 \,\text{GeV} \,,$$

 $m_T^W > 30 \,\text{GeV} \,, \qquad |y_l| < 2.5 \,,$
 $\Delta R_{\mu\mu} > 0.2 \,, \qquad \Delta R_{\mu^{\pm}e} > 0.3 \,,$ (3.4)

with the transverse mass of the W boson defined as

$$m_T^W = \sqrt{2 p_T^e p_T^{\text{miss}} \left(1 - \cos \Delta \Phi_{e,\text{miss}}\right)}.$$
 (3.5)

No veto is applied on additional hadronic activity in the event. Owing to the presence of a single neutrino in the final state, the full kinematics can be reconstructed using an on-shell constraint on the W boson. For this purpose, we adopt the reconstruction method employed in Ref. [1].

WW we examine three different event selection strategies for the WW process. The first is a fully inclusive setup, imposing no kinematic cuts on the final-state leptons and applying no vetoes on jets. The second setup retains the inclusivity in lepton kinematics but incorporates jet vetoes following the ATLAS analysis in Ref. [88], designed to suppress contributions from top-quark and multijet QCD backgrounds through vetoing:

- b-tagged jets with $p_T^b > 20 \,\text{GeV}$ and $|\eta_b| < 2.5$,
- light jets with $p_T^j > 35 \,\text{GeV}$ and $|\eta_j| < 4.5$.

The third configuration implements the full set of fiducial cuts employed in Ref. [88], combining the above jet vetoes with additional lepton-level requirements:

$$p_T^l > 27 \,\text{GeV} \,, \quad p_T^{\text{miss}} > 20 \,\text{GeV} \,, \quad p_T^{e\mu} > 30 \,\text{GeV} \,,$$

 $|y_{\mu}| < 2.5 \,, \qquad |y_e| < 2.47 \,, \qquad m_{e\mu} > 55 \,\text{GeV} \,.$ (3.6)

4 Results

In Tables 2 and 3, we present inclusive and fiducial cross sections for the SM, together with the relevant dimension-6 and dimension-8 operators in the WZ channel for CP-even and CP-odd operators, respectively. The linear and the quadratic contributions of the dimension-6 CP-even operator are denoted as $\mathcal{O}_W^{\text{int}}$ and $\mathcal{O}_W^{\text{sq}}$, respectively. The reported cross sections assume $C_i = 1$ and $\Lambda = 1$ TeV.

σ [fb]	SM	$\mathcal{O}_W^{\mathrm{int}}$	$\mathcal{O}_W^{\mathrm{sq}}$	\mathcal{O}_4	\mathcal{O}_6	\mathcal{O}_{12}	\mathcal{O}_{13}
incl.	$98.37(2)_{-5.1\%}^{+5.3\%}$	$-1.417(1)_{-22\%}^{+26\%}$	$12.43(1)_{-1.1\%}^{+0.9\%}$	$-0.0868(1)_{-4.8\%}^{+5.5\%}$	$-0.0891(3)_{-5.0\%}^{+5.8\%}$	$-1.613(1)_{-5.2\%}^{+5.9\%}$	$1.512(1)_{-5.5\%}^{+6.3\%}$
fid.	$35.34(1)^{+5.6\%}_{-5.6\%}$	$-0.995(2)_{-14\%}^{+16\%}$	$6.575(4)_{-1.6\%}^{+1.6\%}$	$-0.0382(1)_{-5.1\%}^{+5.8\%}$	$-0.0353(2)_{-4.5\%}^{+5.0\%}$	$-0.644(1)_{-5.3\%}^{+6.1\%}$	$0.702(1)_{-5.6\%}^{+6.5\%}$

Table 2: Inclusive (incl.) and fiducial (fid.) WZ cross sections. Shown are the NLO QCD predictions for the SM and for the dimension-6 CP-even operator \mathcal{O}_W —interference (int) and quadratic (sq) contributions, as well as the contributions of the relevant dimension-8 CP-even operators computed at LO. Numbers in parentheses denote MC statistical uncertainties, whilst percentage values correspond to QCD scale variations.

At the inclusive level, we find the dimension-8 contributions to be subdominant with respect to the squared contributions of the dimension-6 operator, $\mathcal{O}_W^{\mathrm{sq}}$, both in the inclusive and fiducial setups of the WZ channel. These conclusions hold for both the CP-even and CP-odd coefficients, as reported in Tables 2 and 3, respectively.

σ [fb]	$\mathcal{O}_{ ilde{W}}^{ ext{int}}$	$\mathcal{O}_{ ilde{W}}^{ ext{sq}}$	\mathcal{O}_5	\mathcal{O}_7	\mathcal{O}_{11}
incl.	$-0.182(3)^{+3.6\%}_{-4.1\%}$	$12.78(1)_{-1.1\%}^{+0.8\%}$	$0.0051(1)_{-5.2\%}^{+6.0\%}$	$0.0044(1)_{-5.8\%}^{+6.7\%}$	$-0.0035(1)_{-3.2\%}^{+2.3\%}$
fid.	$-0.059(1)_{-1.6\%}^{+0.6\%}$	$6.71(1)_{-1.5\%}^{+1.5\%}$	$0.0024(1)_{-5.4\%}^{+6.3\%}$	$0.0018(1)_{-5.7\%}^{+6.6\%}$	$-0.0018(1)_{-1.2\%}^{+1.8\%}$

Table 3: Same as Table 2 but for CP-odd operators.

For the WW channel, Table 4 reports the inclusive cross section in the three setups defined in Section 3, for the SM as well as for the dimension-6 and dimension-8 CP-even operators.

σ [fb]	SM	$\mathcal{O}_W^{\mathrm{int}}$	$\mathcal{O}_W^{\mathrm{sq}}$	\mathcal{O}_{10}	\mathcal{O}_{12}	\mathcal{O}_{13}
incl.	$1895.1(5)_{-11\%}^{+11\%}$	$-8.57(6)_{-15\%}^{+17\%}$	$40.78(9)_{-1.4\%}^{+1.3\%}$	$21.27(1)_{-4.2\%}^{+4.6\%}$	$-5.10(1)_{-4.6\%}^{+5.1\%}$	$4.86(1)_{-4.7\%}^{+5.2\%}$
fid.	$186.8(2)_{-4.8\%}^{+3.6\%}$	$-0.74(5)_{-12\%}^{+14\%}$		$12.06(1)_{-5.8\%}^{+6.7\%}$	$-2.39(1)^{+7.4\%}_{-6.3\%}$	$2.36(1)_{-6.4\%}^{+7.5\%}$
jet-veto-only	$1004.5(3)_{-4.4\%}^{+3.5\%}$	$-0.43(2)_{-66\%}^{+76\%}$	$17.8(2)_{-26\%}^{+19\%}$	$21.27(1)_{-4.2\%}^{+4.6\%}$	$-5.10(1)_{-4.6\%}^{+5.1\%}$	$4.86(1)_{-4.7\%}^{+5.2\%}$

Table 4: Same as Table 2 but for the WW process. Jet-veto-only cross sections are, as expected, identical at LO and differ only at NLO; hence differences appear only in the first three columns.

Overall the dimension-8 contributions are comparatively larger than for WZ. We observe that the contributions from \mathcal{O}_{12} and \mathcal{O}_{13} remain subdominant compared to the squared dimension-6 terms across all setups, whereas the effects of \mathcal{O}_{10} are competitive—particularly in the fiducial and jet-veto-only cases. Further discussion of this behaviour will be provided in the following sections.

4.1 Differential distributions

In this section, we present differential predictions for a selected set of observables:

$$\{m_{4l}, m_{ij}, p_T^X, \phi_i^*, \cos \theta_i^*, \Delta \Phi_{i,j}, \Delta y_{i,j}\},$$
 (4.1)

which correspond, respectively, to the invariant mass of the four-lepton system, the invariant mass of particles i and j, the transverse momentum of particle X, the azimuthal angle and polar angle cosine of particle i, and the azimuthal and rapidity separations between particles i and j.

The polar and azimuthal angles of a selected decay lepton are computed in the rest frame of its parent EW boson, relative to the boson's flight direction in the diboson centre-of-mass (CM) frame. This frame is widely regarded as the natural choice for diboson studies [27, 29–34], as it directly accesses polarisation coefficients defined in the diboson CM frame—commonly adopted in experimental analyses. To fully specify the coordinate system [89], we set the reference/zero axis for the azimuthal angle by aligning it with the decay plane of the Z boson in the diboson CM frame.

Throughout this work, the superscript 'reco.' denotes observables computed with reconstructed information on the missing transverse momentum, p_T^{miss} , whereas the absence of this superscript indicates that truth-level information is used. The treatment of polarisation fractions is more involved in this regard, and we comment on this below.

In Figs. 1 to 6, we present differential predictions for fully leptonic WZ and WW production. The setup of each plot, whether fiducial or inclusive, is indicated at the top of the corresponding panel. In each plot, different colours indicate the SM predictions (SM), interference contributions from the dimension-8 operators denoted as C_i , with $i \in \{4, 5, 6, 7, 10, 11, 12, 13\}$, and the linear and quadratic contributions of the dimension-6 CP-even (CP-odd) operator \mathcal{O}_W (with $W \to \tilde{W}$), denoted as C_W^{int} and C_W^{sq} , respectively. Dashed lines in the plots indicate negative EFT contributions, i.e. destructive interference. Predictions for the SM and the dimension-6 contributions are computed at NLO in QCD, whilst dimension-8 contributions are evaluated at LO. All EFT contributions are shown for coefficient values chosen to produce deviations comparable to those obtained with the dimension-6 coefficient set to unity.

 \mathbf{WZ} Figure 1 illustrates distributions in the invariant mass of the four-lepton system (left) and the transverse momentum of the Z boson (right). Dimension-8 contributions exhibit a

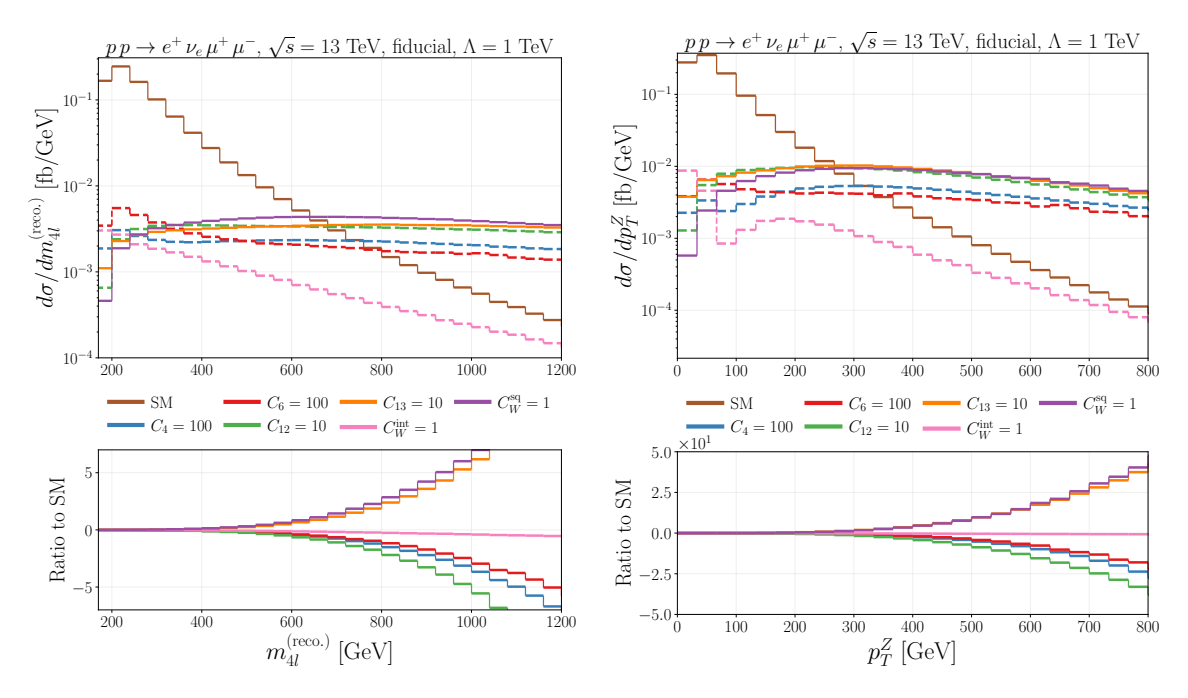


Figure 1: Distributions of the invariant mass of the four-lepton system, m_{4l} , (left) and the transverse momentum of the Z boson, p_T^Z , (right) for WZ production in the ATLAS fiducial setup. Predictions shown include the SM as well as linear and quadratic contributions of the dimension-6 SMEFT operator \mathcal{O}_W computed at NLO in QCD, along with the linear dimension-8 contributions (\mathcal{O}_4 , \mathcal{O}_6 , \mathcal{O}_{12} , \mathcal{O}_{13}) at $\mathscr{O}(\Lambda^{-4})$ computed at LO. The inset displays the ratio of the EFT contributions to the SM. Some coefficients are scaled for visibility. Dashed lines indicate negative contributions.

similar energy dependence as dimension-6 squared contributions, though their magnitude is comparatively insignificant—note the up-scaling of the dimension-8 coefficients by at least

a factor of 10. It should be stressed that throughout, any comparison between dimension-8 and dimension-6 effects implicitly refers to the squared dimension-6 contribution, as it appears at the same order in the EFT expansion as the linear dimension-8 terms. Nevertheless, for completeness, we also present the linear dimension-6 contribution in all the differential distributions, which is of $\mathcal{O}(\Lambda^{-2})$.

Moving to Fig. 2, we present the distributions of the azimuthal angle of the anti-muon (left) and the azimuthal separation between the positron and the anti-muon (right). As in

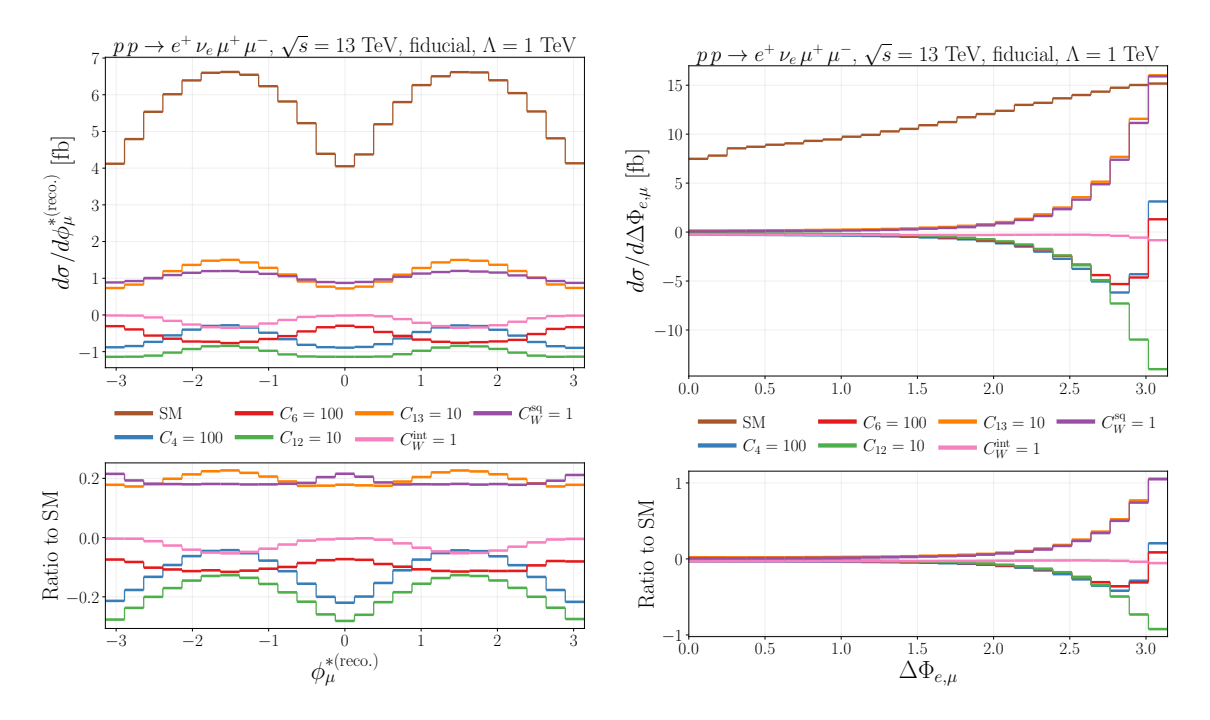


Figure 2: Same as Fig. 1 but for the azimuthal angle of μ (left), and the azimuthal separation between e and μ (right).

previous cases, in the angular observables, we also observe mild effects from the dimension-8 operators. Notably, the contributions of the operators \mathcal{O}_{13} and \mathcal{O}_{12} —with their corresponding WCs scaled to ten times the value of the dimension-6 coefficient C_W —emerges as the most competitive among the dimension-8 contributions across all observables. In the left panel of Fig. 2, we notice that the behaviour of the couples \mathcal{O}_4 , \mathcal{O}_6 and \mathcal{O}_{12} , \mathcal{O}_{13} differs from the other observables. Specifically, \mathcal{O}_4 and \mathcal{O}_6 oscillate with the same frequency, but with different amplitude modulations, whilst the modulation of \mathcal{O}_{12} and \mathcal{O}_{13} differs by an offset. It is worth noting that, whilst the distribution shapes induced by \mathcal{O}_{12} and \mathcal{O}_{13} exhibit certain differences, the two coefficients can still display a strong correlation in a joint fit when all bins are considered, owing to the overall symmetry of the distribution across the full range. However, a fit based on a particular combinations of bins breaks the degeneracy, a similar behaviour is observed for \mathcal{O}_4 and \mathcal{O}_6 . In the right panel of Fig. 2 we observe that the contribution induced by \mathcal{O}_4 and \mathcal{O}_6 exhibit a sudden suppression of the cross section as $\Delta\Phi_{e,\mu}$ approaches π . This behaviour can be attributed to non-trivial cancellations between different regions of phase space where the differential cross-section takes opposite signs—cf.

the left panel of Fig. 3.

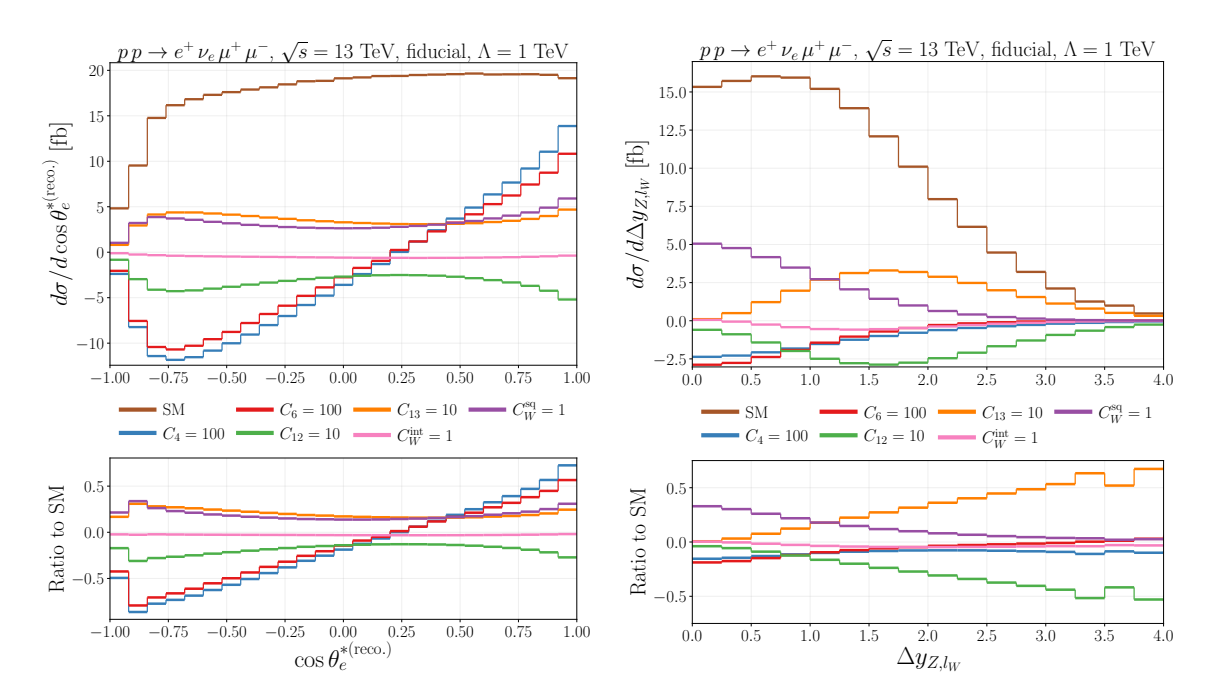


Figure 3: Same as Fig. 1 but for the polar angle of e (left), and the rapidity separation between Z and the lepton l from the W decay, l_W , (right).

Turning to the polar decay angle distribution in the left panel of Fig. 3, we observe a similar pattern to that discussed previously: dimension-8 effects remain generally sub-dominant, with the operators \mathcal{O}_4 and \mathcal{O}_6 exhibiting a sign change in their interference contributions. Finally, in the right panel of Fig. 3, the rapidity separation observable exhibits significant shape distortions induced by \mathcal{O}_{12} and \mathcal{O}_{13} , relative to both the SM and \mathcal{O}_W . This results in distinct two-dimensional shapes in the fit, leading to comparatively enhanced constraining power relative to the other observables—to be discussed later.

Finally, in Fig. 4, we show the distributions of the azimuthal angle of the positron, including CP-odd contributions. The left and right panels correspond to predictions obtained using truth-level and reconstructed information on the missing transverse momentum, respectively. Both plots are presented in the inclusive setup. CP-odd contributions are generally negligible compared to their CP-even counterparts. Notably, the contribution from \mathcal{O}_{11} yields an amplitude that is an order of magnitude larger than those from \mathcal{O}_{5} and \mathcal{O}_{7} . However, upon integrating over the full angular domain, cancellations across phase-space regions suppress the total cross section, so the net contributions of all CP-odd operators are of the same order; see Table 3.

 $\mathbf{W}\mathbf{W}$ in contrast to WZ production, the WW channel exhibits a larger cross section but introduces considerable challenges in the fully leptonic decay mode. The dominant top-quark backgrounds produce the same final-state topology as the signal, complicating the isolation of WW events. Furthermore, the two undetected neutrinos greatly restrict the

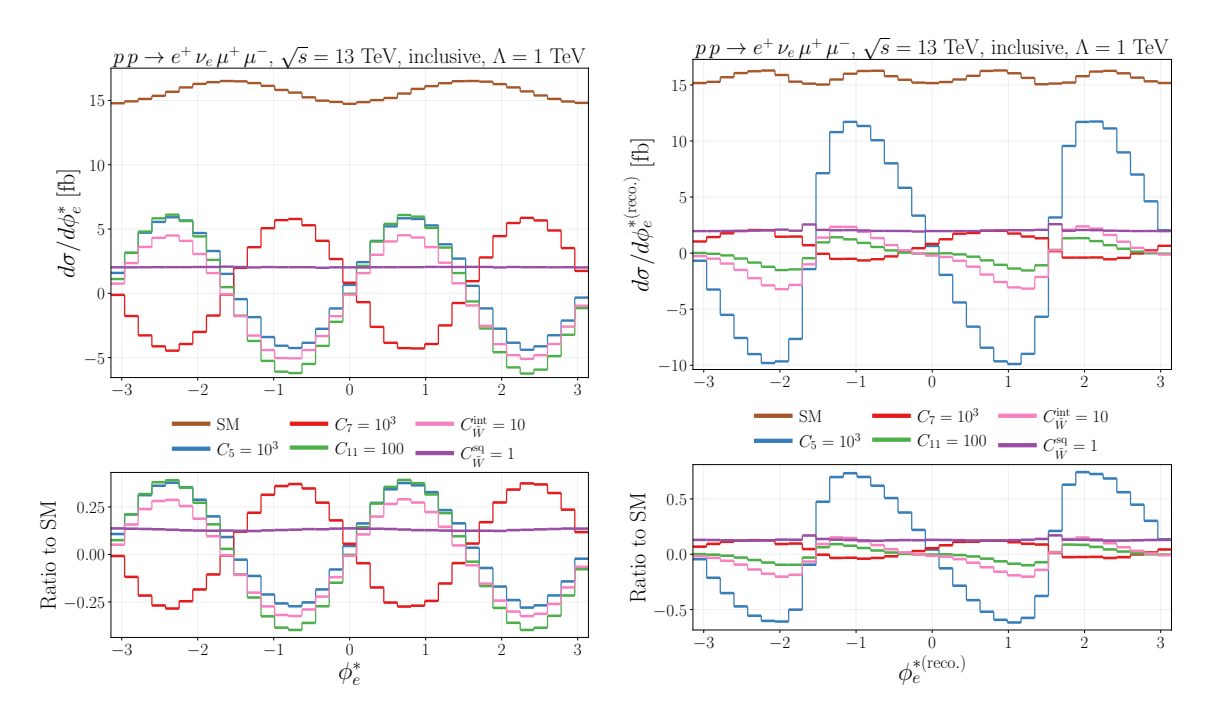


Figure 4: Differential cross sections in the azimuthal angle of *e*, including contributions from CP-odd dimension-6 and dimension-8 operators. Both panels correspond to the inclusive setup: the left plot uses truth-level information for the missing transverse momentum, whilst the right plot is based on reconstructed information.

number of measurable differential observables, making it impossible to reconstruct the rest frame of a single W boson.

In Figs. 5 and 6, we present differential predictions for the dilepton invariant mass, $m_{e\mu}$ and the azimuthal separation, $\Delta\Phi_{e,\mu}$, respectively, in the fiducial (left panels) and the fully inclusive (right panels) setups of fully leptonic WW production. The fiducial selection corresponds to the third configuration described earlier for WW production in Section 3. Unlike in the WZ analysis, here we also present predictions for dimension-6 effects at LO, for reasons that will be clarified later.

Notably, we observe that the dimension-8 operator \mathcal{O}_{10} exhibits a competitive effect compared to the quadratic dimension-6 contribution, particularly pronounced in the back-to-back regions and in the high-energy tails. However, this effect is more evident in the fiducial setup. The reason can be attributed to the jet-veto effect in the fiducial setting. As has also been concluded in previous studies, see for e.g. [57], and whilst the jet-veto application is necessary for the background suppression in WW production, the quadratic EFT contributions at NLO are significantly smaller than the LO ones. This is due to the jet veto significantly suppressing the NLO real emissions. Such an effect is crucial in this study, whose primary objective is to compare the quadratic contributions from dimension-6 to the linear contributions from dimension-8 operators. Moreover, it also motivates the study of dimension-8 effects at NLO in QCD which we postpone for future work.

Finally, we observe that the contributions from \mathcal{O}_{12} and \mathcal{O}_{13} exhibit similar behaviour.

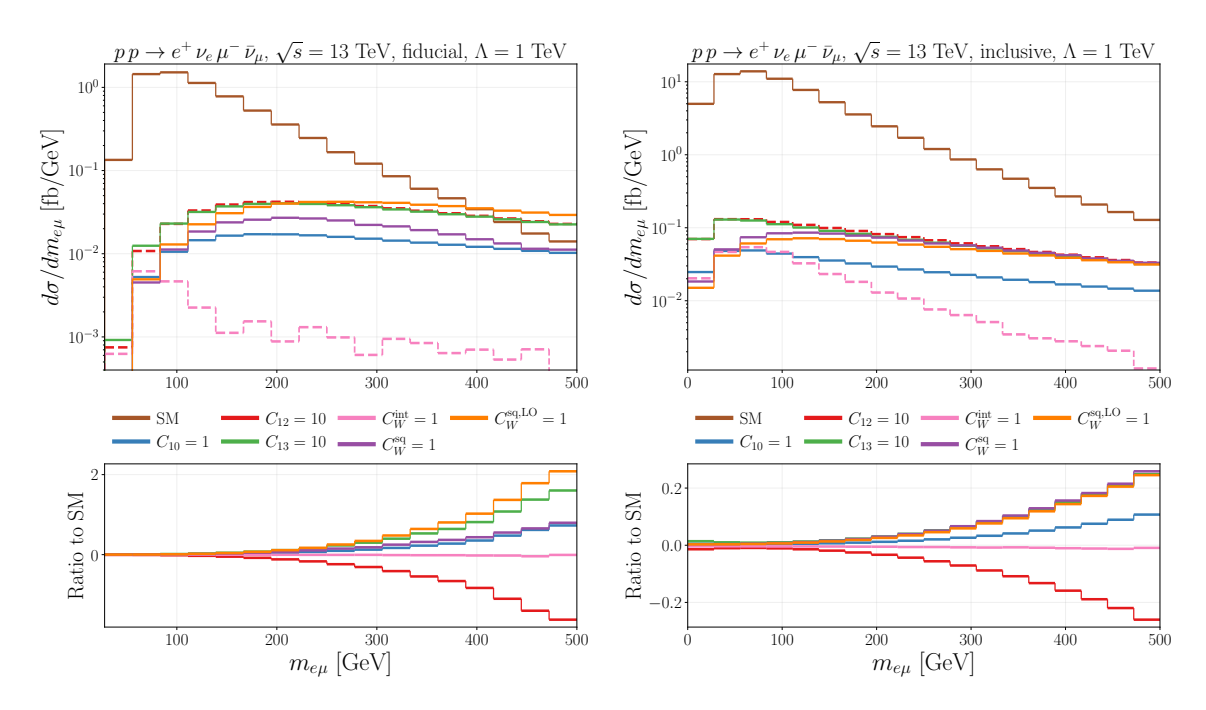


Figure 5: Distributions of the dilepton invariant mass, $m_{e\mu}$, in WW production in the ATLAS fiducial (left) and the fully inclusive setup (right). The structure of the figure is similar to that of Fig. 1.

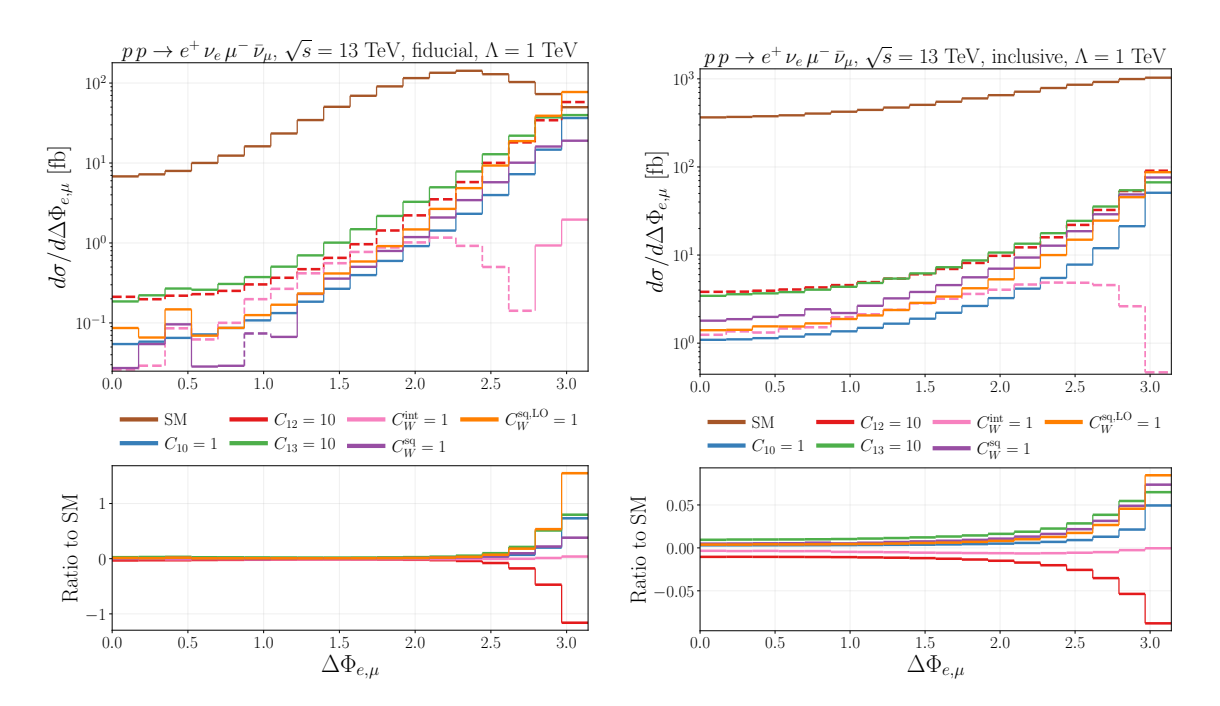


Figure 6: Same as Fig. 5 but for the azimuthal separation between the leptons, $\Delta \Phi_{e,\mu}$.

This is expected, as the leading high-energy contribution of those operators to the interference with the SM scales with the linear combination $(C_{12} - C_{13})$ [54]. As a result, any

differences between the two operators arise from subleading terms, which become relevant only in the low-energy bins of the distributions. This observation holds for both WW and WZ, although it is more pronounced in the latter.

4.2 Polarisation fractions

We now shift focus to angular observables in boson decays, which are particularly sensitive to interference effects and probe the polarisation of the gauge bosons. In the absence of any selection cuts on the leptons, and assuming access to MC truth-level momenta, i.e. without neutrino reconstruction, the differential decay rate of an electroweak boson into two final-state particles can be expressed as follows:

$$\frac{1}{\sigma} \frac{d\sigma}{d\cos\theta^* d\phi^*} = \frac{3}{16\pi} \left[1 + \cos^2\theta^* + \frac{A_0}{2} (1 - 3\cos^2\theta^*) + A_1\sin 2\theta^* \cos\phi^* + \frac{1}{2} A_2\sin^2\theta^* \cos 2\phi^* + A_3\sin\theta^* \cos\phi^* + A_4\cos\theta^* + A_5\sin\theta^* \sin\phi^* + A_6\sin 2\theta^* \sin\phi + A_7\sin^2\theta^* \sin 2\phi^* \right], (4.2)$$

where ϕ^* and θ^* are, respectively, the azimuthal and polar angles of one of the decay leptons. Upon integration over the azimuthal decay angle, the decay rate reads:

$$\frac{1}{\sigma} \frac{\mathrm{d}\sigma}{\mathrm{d}\cos\theta^*} = \frac{3}{8} \left(1 + \cos^2\theta^* + \frac{A_0}{2} \left(1 - 3\cos^2\theta^* \right) + A_4\cos\theta^* \right). \tag{4.3}$$

Through linear combinations of the coefficients A_0 , A_4 , this expression can be re-written in terms of polarisation fractions:

$$\frac{1}{\sigma} \frac{d\sigma}{d\cos\theta^*} = \frac{3}{8} \left[2 f_0 \sin^2 \theta^* + f_L \left(1 + \cos^2 \theta^* - 2 c_{LR} \cos \theta^* \right) + f_R \left(1 + \cos^2 \theta^* + 2 c_{LR} \cos \theta^* \right) \right], \tag{4.4}$$

where f_0 , f_R , f_L are the longitudinal, right-handed, and left-handed polarisation fractions, respectively. The parameter c_{LR} characterises the interplay between left- and right-handed couplings of the EW boson to massless leptons, effectively quantifying their relative contribution;

$$c_{\rm LR} = \frac{|g_{\rm L}|^2 - |g_{\rm R}|^2}{|g_{\rm L}|^2 + |g_{\rm R}|^2},\tag{4.5}$$

which are unaffected by the SMEFT operators considered in this work and are therefore fixed to their SM values:

$$c_{\text{LR}}^W = 1$$
, $c_{\text{LR}}^Z = \frac{1 - 4\sin^2\theta_W}{1 - 4\sin^2\theta_W + 8\sin^4\theta_W} \approx 0.215$, $\sin^2\theta_W = 1 - \frac{m_W^2}{m_Z^2}$. (4.6)

The A_0 and A_4 coefficients are extracted from Eq. (4.3) and they are directly related to the longitudinal- and transverse-polarisation fractions through the following relations:

$$A_0 = 2 f_0, \qquad A_4 = 2 c_{LR} (f_R - f_L).$$
 (4.7)

The angular coefficients A_0 and A_4 , and consequently, the corresponding polarisation fractions, are shown in Fig. 7 as functions of all CP-even dimension-6 and dimension-8 coefficients relevant to WZ production. The corresponding CP-odd results are negligible due to the numerically insignificant contributions of the considered SMEFT operators and therefore, are not shown. The dependence of the angular coefficients is parametrised as follows. For a given angular coefficient A_i , two truncations of the SMEFT expansion are considered: one at linear order and one including quadratic terms—with the dimension-8 contribution entering at $\mathcal{O}(\Lambda^{-4})$:

$$A_i^{(1)}(\lambda_j) = \frac{A_i^{\text{SM}} + \lambda_j A_i^{\text{int}} \kappa^{\text{int}}}{1 + \lambda_j \kappa^{\text{int}}}, \quad A_i^{(2)}(\lambda_j) = \frac{A_i^{\text{SM}} + \lambda_j A_i^{\text{int}} \kappa^{\text{int}} + \lambda_j^2 A_i^{\text{sq}} \kappa^{\text{sq}}}{1 + \lambda_j \kappa^{\text{int}} + \lambda_j^2 \kappa^{\text{sq}}}, \tag{4.8}$$

where

$$\kappa^{\text{int}} = \frac{\sigma^{\text{int}}}{\sigma^{\text{SM}}}, \qquad \kappa^{\text{sq}} = \frac{\sigma^{\text{sq}}}{\sigma^{\text{SM}}}, \qquad j \in \{W, 4, 6, 12, 13\}.$$
(4.9)

and we defined

$$\lambda_W = \frac{C_W}{\Lambda^2}, \qquad \lambda_n = \frac{C_n}{\Lambda^4}, \ n \in \{4, 6, 12, 13\}.$$
 (4.10)

The results are reported for WZ production in an inclusive setup, using truth-level MC information for the missing transverse momentum. We emphasise that extracting these coefficients via spherical–harmonics projections, i.e. Eq. (4.3), is well defined only without fiducial cuts on decay products and with perfect neutrino reconstruction, which allows full integration over the decay angles. In a fiducial setup with realistic neutrino reconstruction, applying the same strategy can yield unphysical results [26, 89–91].

We consider two different setups. The first is a fully inclusive configuration and the second applies a lower cut on the transverse momentum of the EW boson, $p_T^V > 400$ GeV. In the second case, we focus on the boosted regime in which the effects of SMEFT operators are more pronounced. The results are shown in Fig. 7 for a new physics scale of $\Lambda = 3$ TeV, at which quadratic contributions of the dimension-8 operators are negligible.

In the top panel of Fig. 7, which shows results for the inclusive setup, we observe that the contributions from dimension-8 operators to the angular coefficients are negligible, whilst the dimension-6 operators induce only small deviations. This behaviour is a consequence of the suppressed contributions of $\kappa^{\rm int}$ and $\kappa^{\rm sq}$ when $\Lambda=3$ TeV. As a result, the polarisation fractions remain very close to the SM prediction.

In the bottom panel, for the boosted scenario, we observe that the dimension-6 operator has a large impact and the contributions from dimension-8 operators become non-negligible. In both the left and right panels, and focusing on $A_0^{(1)}$ for the dimension-8 operators, the slope of the line is dominated by the denominator of Eq. (4.8). This indicates that the angular coefficient A_0^{int} which corresponds to the interference of the dimension-8 amplitude with the SM is negligible. This observation is consistent with the findings of Ref. [54], where the corresponding helicity amplitudes were studied and it was shown that the production of longitudinal vector bosons is suppressed compared to transverse ones, vanishing in the case of the operators \mathcal{O}_{12} and \mathcal{O}_{13} for the production of two longitudinal bosons. Turning to $A_4^{(1)}$, we find a different behaviour: as the vector bosons produced with an insertion of the

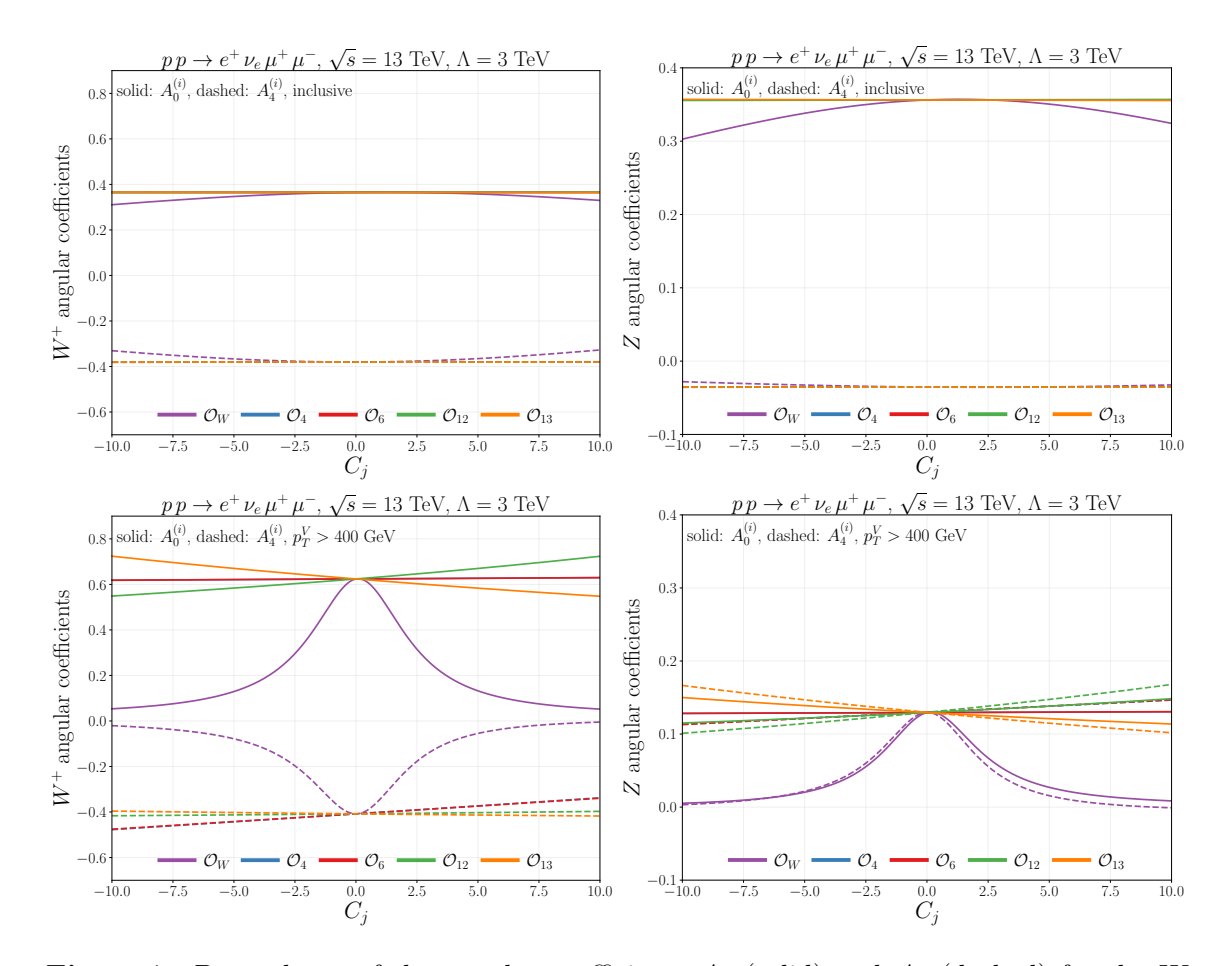


Figure 7: Dependence of the angular coefficients A_0 (solid) and A_4 (dashed) for the W boson (left) and the Z boson (right) in WZ production on the Wilson coefficients of CP-even operators. Top panels are computed for an inclusive setup, while bottom panels are computed with a minimal cut on the p_T of the EW boson of 400 GeV. The parametrisation is given in terms of $A_i^{(2)}$, shown for the dimension-6 operator \mathcal{O}_W including both linear and quadratic terms, and $A_i^{(1)}$, shown for the dimension-8 operators retaining only the linear contributions.

dimension-8 operators are mostly transversely polarised, their contribution to the angular coefficient A_4 is mild, but not negligible. We also comment on the dimension-6 operator which leads mostly to transverse bosons, with A_0 and thus f_0 tending to zero for large coefficients where the EFT contribution dominates.

Furthermore, we note the degeneracy between the coefficients (C_4, C_6) and (C_{12}, C_{13}) , consistent with what was already observed in the differential distributions. This degeneracy is most apparent in the bottom panel. Finally, concerning the Z-boson panel (right), we observe that, unlike in the W case, the Z boson exhibits nearly equal left- and right-handed polarisation fractions in the inclusive setup, which results in a much smaller value of A_4 , as expected. Moving to the boosted setup, and focusing on the right panel, we observe that the values of A_0 and A_4 become very close, with A_0 being suppressed and A_4 enhanced.

This leads to a reduction in the longitudinal polarisation fraction of the Z boson, and to an excess of right-polarised over left-polarised bosons.

5 Sensitivity study

Using a statistical approach based on a χ^2 analysis, we combine experimental measurements and SMEFT predictions to derive constraints on the Wilson coefficients considered in this work. We employ differential data from multiple observables and kinematic regions. Angular observables that are sensitive to the polarisation structure of the diboson events are also included. The total experimental uncertainties are computed as the quadrature sum of statistical errors and systematic uncertainties. Since we assume uncorrelated errors, we introduce an additional 5% systematic uncertainty, applied bin-by-bin, as a conservative measure.

We adopt SM predictions as used in ATLAS analyses: NNLO QCD for the WZ [4] and NNLO QCD combined with NLO EW corrections for WW production [5, 9]. Within the fiducial WZ region under consideration [1, 3], NLO EW corrections amount to about -3% relative to NNLO QCD results [9, 29]; thus, their omission is unlikely to significantly affect our fits. The SM predictions are extracted by digitising plots presented in experimental papers, as numerical results were not available in the HEPData database [92].

By performing a χ^2 fit, we establish individual and marginalised 95% confidence level (CL) intervals for the WCs, quantifying the agreement of the SMEFT predictions with data. Our bounds apply exclusively within experimentally defined fiducial regions. Our EFT theoretical predictions are computed as described in Section 3.

Our analysis considers the EFT parametrisation up to $\mathcal{O}(\Lambda^{-4})$. It is worth noting that we have explicitly checked the contributions arising from the squared terms of dimension-8 operators. We find that, for coefficients of order one to ten, i.e. $C = \mathcal{O}(1-10)$, and in the region where the cut-off scale is of order 3 TeV or higher such contributions are subdominant.

WZ we make use of the fiducial differential cross section data provided by the ATLAS collaboration [1, 3]. The considered differential measurements include the following observables:

$$\{p_T^Z, p_T^W, m_T^{WZ}, \Delta\Phi_{W,Z}, p_T^{\nu}, |\Delta y_{Z,l_W}|, \cos\theta_e^*\}.$$
 (5.1)

For the polar decay angle, $\cos \theta_e^*$, we use EFT predictions corresponding to its reconstructed definition, following the neutrino reconstruction method implemented by ATLAS [1]. We highlight that all differential observables, with the exception of $\cos \theta_e^*$, are taken from Ref. [1], based on data corresponding to an integrated luminosity of 36.1 fb⁻¹. In contrast, the polar decay angle data are extracted from Ref. [3], which uses a larger dataset with an integrated luminosity of 139 fb⁻¹.

WW we employ the differential measurements reported by ATLAS in Ref. [88]. The analysis incorporates several kinematic distributions:

$$\{p_T^{l_{\text{lead.}}}, \quad p_T^{e\mu}, \quad m_{e\mu}, \quad \Delta\Phi_{e,\mu}, \quad |y_{e\mu}|, \quad \left|\tanh\frac{\Delta\eta_{e,\mu}}{2}\right|\},$$
 (5.2)

from which we extract bounds using the first three measurements. The remaining distributions exhibit systematic discrepancies between data and SM predictions—specifically, a consistent underestimation of the fiducial cross sections by 15–20% as noted in Ref. [88]. Due to this modelling tension, we do not consider the resulting bounds from these observables reliable for constraining SMEFT effects and therefore exclude them from our results.

HL-LHC projections experimental central values are assumed to coincide with the SM predictions. Statistical uncertainties are rescaled according to the luminosity, whilst systematic uncertainties are uniformly reduced by a factor of two.

5.1 Fit method and results

Throughout our analysis, all operator coefficients are scanned within the range $C_i \in [-10, 10]$ to remain within the perturbative regime but allowing also strongly coupled UV complete models¹. At cut-off scales $\Lambda \geq 3$ TeV, the resulting dimension-8 constraints become weaker than the imposed prior and are therefore regarded as unconstrained, with the exception of the coefficient C_{10} in the WW channel. The corresponding bounds on C_{10} in WW production at $\Lambda = 3$ TeV, extracted from the three observables under consideration and based on current LHC data, are reported in Table 5. Results for different values of Λ are presented in Tables 8 and 9 of Section A.

obs	C_W^{LO} , ind	C_W , ind	C_{10} , ind	C_W , marg
$p_T^{l_{\mathrm{lead.}}}$	[-1.45, 1.42]	[-2.60, 2.81]	[-2.50, 7.41]	[-4.33, 4.54]
$p_T^{e\mu}$	[-1.63, 1.58]	[-3.13, 3.30]	-	[-4.09, 4.23]
$m_{e\mu}$	[-1.96, 1.96]	[-4.73, 5.00]	-	[-6.78, 7.04]

Table 5: Individual (ind) bounds on the dimension-6 coefficient C_W and the dimension-8 coefficient C_{10} in the WW channel, shown for each of the observables (obs) considered with current LHC data. For the dimension-6 coefficient, bounds are presented at LO and NLO. The last column reports the marginalised (marg) bounds for C_W at NLO. All bounds are extracted at $\mathcal{O}(\Lambda^{-4})$ and assume a cut-off scale of $\Lambda = 3$ TeV. The '-' indicates the coefficient is unconstrained within the imposed prior.

In Table 5, the looser bounds at NLO can be attributed to jet-veto effects in the WW channel, as discussed in Ref. [57], and can be understood as a consequence of the less-than-unity K-factors in the fiducial setup shown in Fig. 5. As previously mentioned, the coefficient C_{10} receives a meaningful individual constraint from $p_T^{l_{\text{lead}}}$ even for $\Lambda = 3$ TeV. This observation is consistent with the findings of Ref. [54], which emphasise the importance of the operator \mathcal{O}_{10} . Finally, we note that the marginalised bounds on C_W at NLO differ significantly from the individual ones; this feature also appears in the WZ channel—marginalised and individual bounds from the latter are presented in Tables 6 and 7 of Section A—and will be discussed in detail in the following section.

¹More sophisticated priors on the Wilson coefficients can be applied by employing arguments based on particular UV dynamics, see for example Refs. [93, 94].

Our results agree with the findings of Ref. [61]. We find that, even in a quadratic analysis of diboson observables, it is not possible to simultaneously remain within the weakly coupled regime and satisfy the EFT validity condition. When ensuring that the energy probed is significantly smaller than the cut-off scale Λ , the bounds obtained on C_W enter in the strong coupling regime.

5.2 Impact of dimension-8 operators in the fit

To illustrate more clearly the impact of including dimension-8 operators in the fit, we present the ratio of the widths of the marginalised to the individual bounds on the dimension-6 coefficient C_W . The marginalised bounds on C_W at various cut-off-scales are presented in Tables 6 and 8 of Section A. The results are shown, respectively, for WZ and WW production with current LHC data in Figs. 8 and 10, and for the HL-LHC projections in Figs. 9 and 11. Each marker on the plot indicates the used new-physics scale Λ ranging from 3 to 5 TeV. Results are displayed for each observable. The heat-map indicates the stringency of the individual bounds.

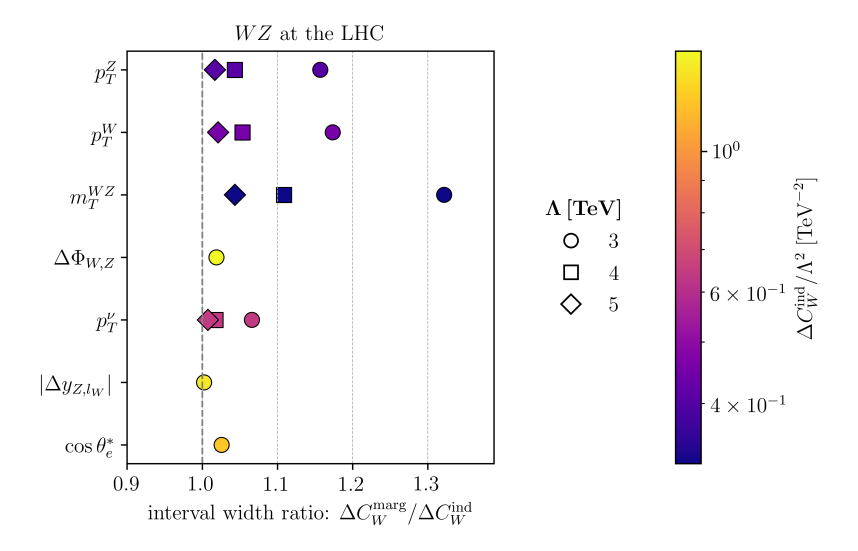


Figure 8: Shown for each observable at different new-physics scales Λ —denoted by the different marker shapes—is the ratio between the widths of the marginalised and individual bounds of the dimension-6 coefficient C_W at NLO. The colour scale indicates the stringency of the individual bounds. All results are at $\mathcal{O}(\Lambda^{-4})$ in the EFT parametrisation.

For a given observable, the overlap of the markers at a ratio close to unity implies that, for such observables, bounds on the dimension-6 coefficients can be reliably extracted independently of whether or not the relevant dimension-8 operators are included. In Figs. 8 and 9, we observe that, in the WZ channel, both with the current LHC data and with the HL-LHC projections, in a fit that does not include dimension-8 operators, the observables $\Delta\Phi_{W,Z}$, $\Delta y_{Z,\ell_W}$ and $\cos\theta_e^*$ can be reliably used to extract bounds on C_W . It is worth noting that only the ratios at 3 TeV are shown for the aforementioned angular observables.

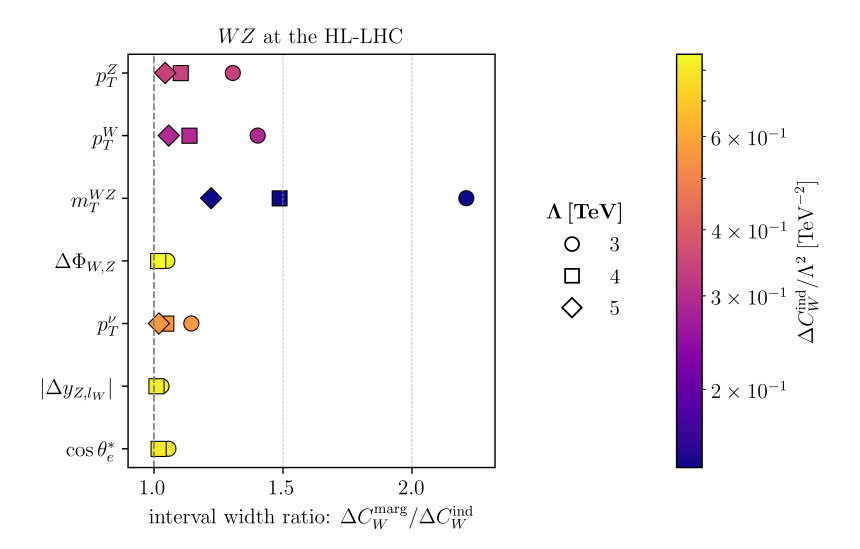


Figure 9: Same as Fig. 8 but for the HL-LHC projections.

At higher cut-off scales, within the allowed scanning range of the fit, the coefficient C_W remains unconstrained.

The situation is different for dimensionful observables: extracting bounds, at 3 TeV, is not robust under the inclusion of dimension-8 operators, since the ratio of marginalised to individual bounds can induce a $\sim 15\%$ change for p_T^Z and around $\sim 30\%$ for m_T^{WZ} for the LHC case. We note here that the transverse mass generally yields the most stringent bound among all observables. At higher cut-off scales, i.e. at 5 TeV, these observables are expected to provide more reliable constraints in a dimension-6-only analysis. These conclusions remain qualitatively the same in the HL-LHC case.

Moving to the WW channel in Figs. 10 and 11, for the current LHC data and the HL-LHC projections, respectively, it is evident that the impact of dimension-8 operators is more significant relative to the WZ case. This is not surprising given the importance of \mathcal{O}_{10} . Considering the most stringent observable $p_T^{l_{\rm lead}}$ and a cut-off scale of 3 TeV, neglecting dimension-8 effects can induce uncertainties as large as 60% in the LHC case.

Furthermore, we observe that the dilepton invariant mass is not a reliable observable for the extraction of bounds in the LHC case. Using this observable with the current LHC data, the coefficient C_W remains unconstrained beyond 3 TeV, and the only available constraint carries an error of nearly 40% in a dimension-6-only analysis—as seen in Fig. 10. In the HL-LHC scenario in Fig. 11, by contrast, the coefficient is constrained at higher cut-off scales beyond 3 TeV.

Finally, it is worth noting that in the HL-LHC projections, the ratios of marginalised to individual bounds are generally larger than in the LHC case. This suggests that the impact of dimension-8 operators will remain non-negligible at higher luminosities, and may even become more pronounced than at the LHC.

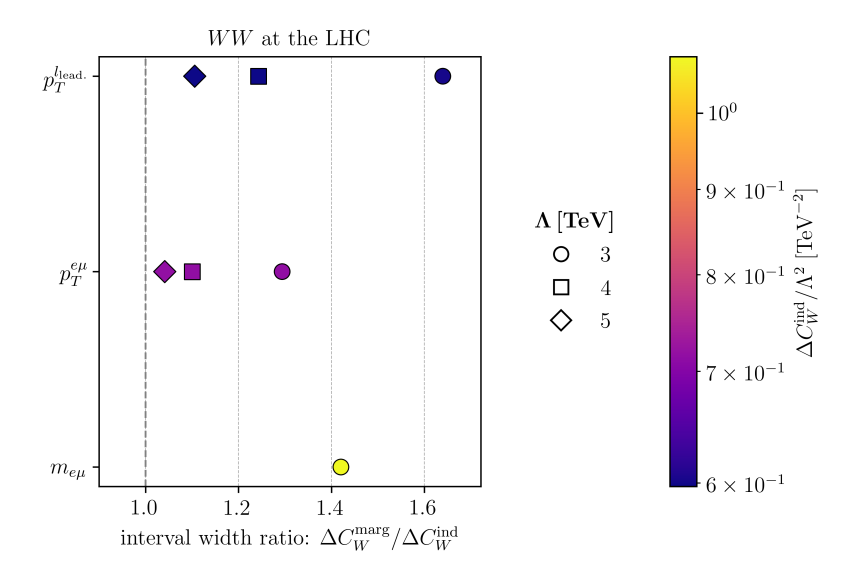


Figure 10: Same as Fig. 8 but for the WW channel.

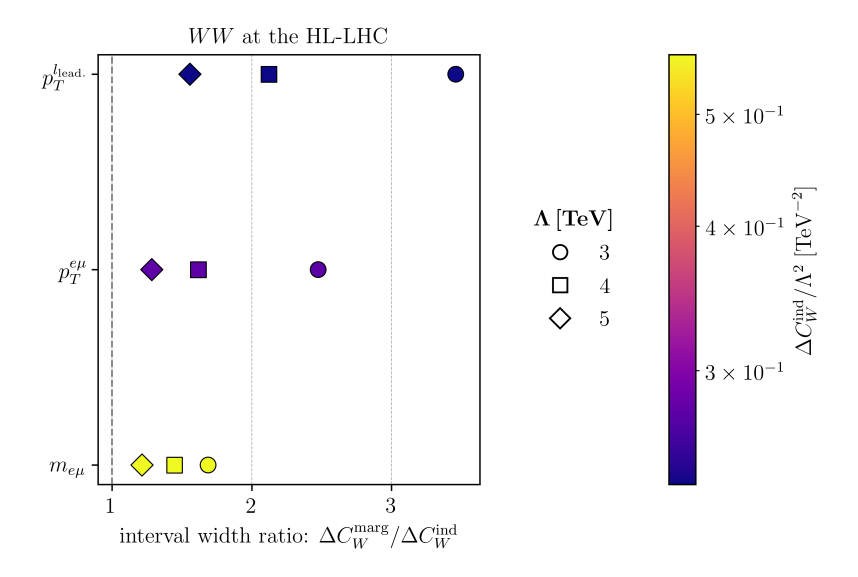


Figure 11: Same as Fig. 10 but for the HL-LHC projections.

5.3 Two-dimensional scans

In this section, we aim to assess possible degeneracies between the operators we consider and thus we present the two-dimensional fits for the WZ and WW channels in Figs. 12 and 13, respectively. The fit retains terms up to $\mathcal{O}(\Lambda^{-4})$ in the EFT expansion, and includes all the relevant dimension-6 and dimension-8 CP-even coefficients. The joint-probability scans include only a selected subset of observables for WZ, together with the contour corresponding to their combination. We emphasise that the latter is a simplified combination, assuming no bin-to-bin or cross-distribution correlations.

For the WZ case shown in Fig. 12, one can immediately identify flat directions arising

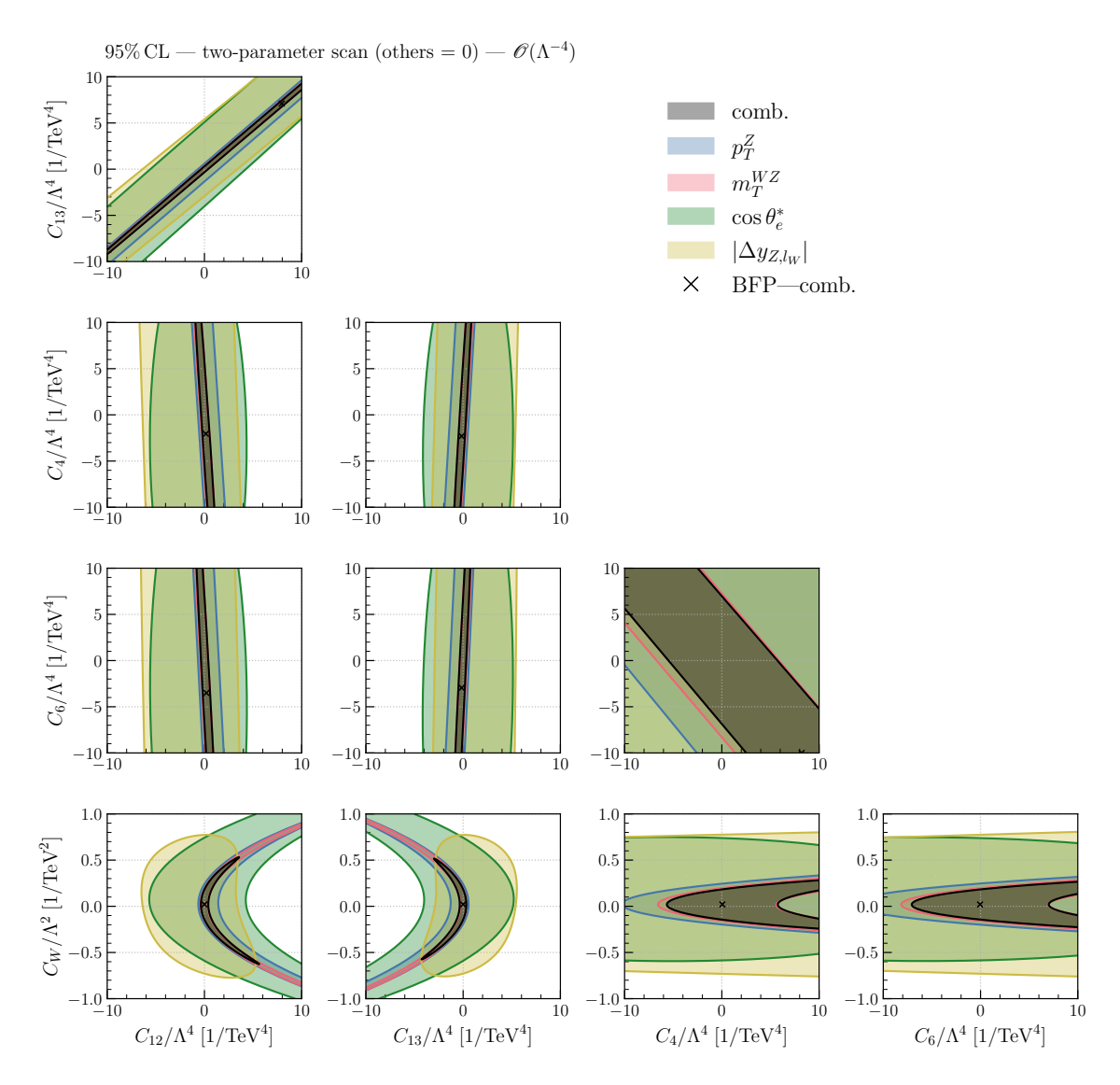


Figure 12: Two-dimensional fits for the CP-even dimension-6 and dimension-8 coefficients in the WZ channel. Shown are the constraints from a selected set of observables individually, as well as from their combination. The EFT parametrisation includes linear contributions in dimension-8 as well as linear and quadratic contributions in dimension-6, i.e. $\mathcal{O}(\Lambda^{-4})$. The best-fit point (BFP) of the combined fit is indicated.

between the pairs (C_4, C_6) and (C_{12}, C_{13}) . Across the board, m_T^{WZ} is the observable with the strongest constraining power. An interesting feature appears in the scan of dimension-6 coefficient, C_W , vs the dimension-8 ones, C_{12} and C_{13} : the contour arising from $\Delta y_{Z,l_W}$ exhibits a markedly different shape compared to the other observables. Since these joint probability scans essentially probe the shape dependence of the observables, we attribute this behaviour to the corresponding distribution shown in the right panel of Fig. 3. There, the rapidity separation at dimension-8 displays a distinctly different shape compared to both dimension-6 and the SM predictions. This feature is not observed, for instance, for

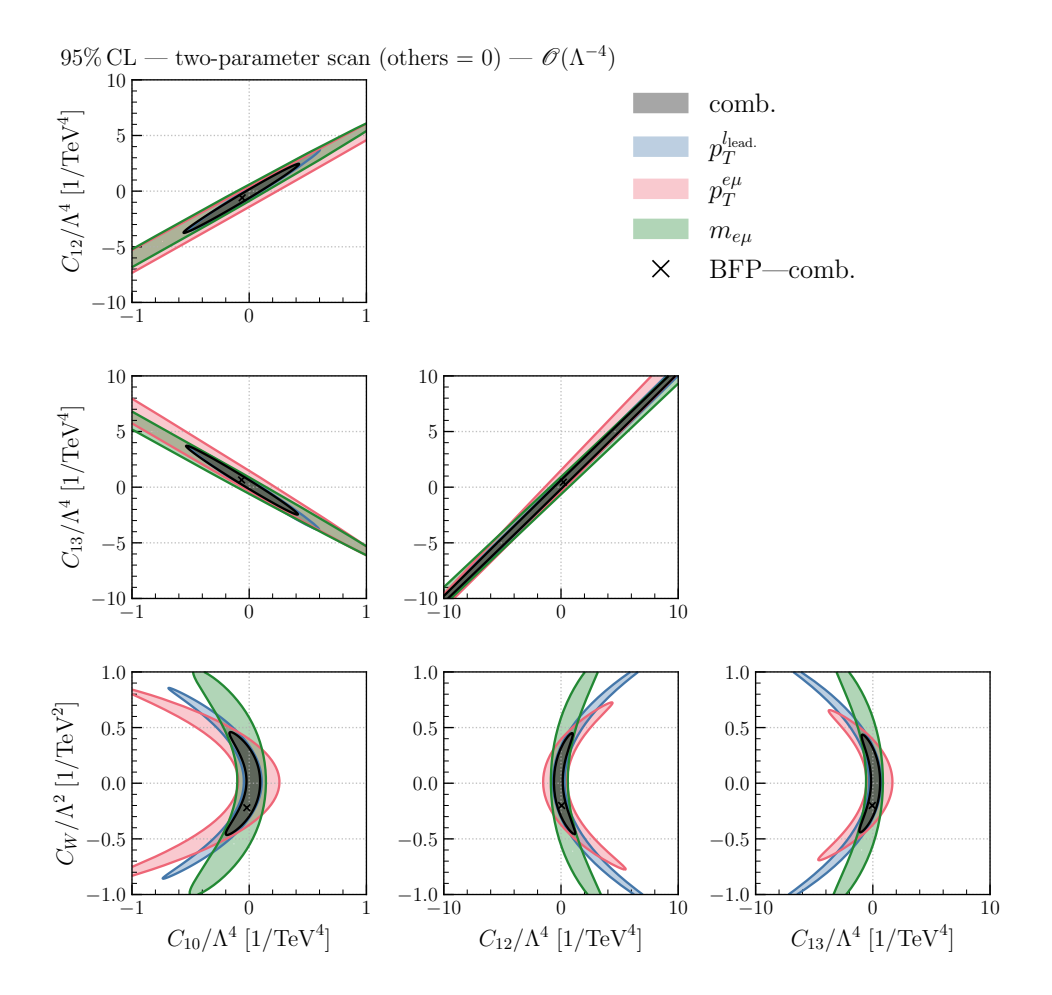


Figure 13: Same as Fig. 12 but for the WW process.

the operators \mathcal{O}_4 and \mathcal{O}_6 where observe a correlation between either of C_4 or C_6 and the dimension-6 coefficient C_W in the case of $\Delta y_{Z,\ell_W}$.

Finally, for the $\cos \theta_e^*$ observable, we observe that, unlike the other cases, the corresponding contour exhibits a broken correlation between C_W and the dimension-8 coefficients C_4 and C_6 , as well as between $C_{4,6}$ and $C_{12,13}$. This behaviour can be understood from the left panel of Fig. 3, where the distinctive shape of each contribution is clearly visible and manifests in the fit.

In Fig. 13 for the WW channel, a correlation is again observed in the (C_{12}, C_{13}) pair across all observables. Furthermore, for each of their scan with C_{10} , the transverse momentum of the leading lepton is observed to have the largest constraining power, in line with our findings in Table 5. In the dimension-6 scan, the strong constraining power of C_{10} is once more manifest, with all observables competing to provide the most stringent bounds. For the dimension-6 scan against the pair (C_{12}, C_{13}) , the contours are mirrored, as expected from the behaviour of these operators in the differential predictions, see for example, Fig. 5.

6 Conclusions

In this work, we studied diboson production, namely the WZ and WW processes, in the SMEFT framework, including the relevant dimension-6 and dimension-8 CP-even and CP-odd operators. We first classified the dimension-8 operators according to their high-energy behaviour and identified the subset that induces non-negligible effects. In doing so, we significantly reduced the number of dimension-8 operators entering the analysis and established that CP-odd effects remain negligible throughout.

We then computed SMEFT predictions at both the inclusive and differential crosssection level for all relevant operators in both channels, using a set of observables commonly employed in experimental analyses. Several noteworthy features were observed. In the WZ channel, the linear dimension-8 terms are subdominant compared to the squared dimension-6 ones for $\mathcal{O}(1)$ coefficients and $\Lambda=1$ TeV. In contrast, in the WW channel, the contributions of the dimension-8 operator \mathcal{O}_{10} are competitive with those from the dimension-6 operator.

In addition, we computed the angular coefficients directly related to the longitudinal and transverse polarisation fractions, and thereby quantifying the impact of dimension-8 operators on the vector-boson polarisation. We found negligible effects for a fully inclusive setup and mild, but non-negligible effects, for the production of transverse polarised bosons in the region $p_T^V > 400$ GeV. Furthermore, certain degeneracies between pairs of dimension-8 coefficients, previously identified in the differential distributions, were also reflected in this study.

Furthermore, we employed a χ^2 fit to assess the impact of the different operators in constraining the corresponding coefficients. Using data from the ATLAS and CMS experiments, we compared our theoretical predictions at both the inclusive and differential level, performing both individual and marginalised fits. Our fit corroborates the earlier findings, namely that C_{10} is relatively competitive in the WW channel. We then assessed the effect of including or omitting dimension-8 operators in the fit. In this exercise, the marginalised bounds on the dimension-6 coefficient C_W differed non-negligibly from the corresponding individual ones even for new physics scales of 3 TeV, underscoring the importance of including dimension-8 operators in a global fit scenario in a UV agnostic setup. We provided summary plots that encode which observables can be used reliably to extract bounds in analyses neglecting dimension-8 effects, and, in contrast, which observables require the inclusion of dimension-8 contributions in a marginalised fit.

Finally, we presented two-dimensional scans for pairs of coefficients: for a selected set of observables in the WZ channel and for all observables in the WW channel. We also showed the contours corresponding to the combination of these observables. These results again confirmed our earlier findings, namely the presence of flat directions between the pairs of dimension-8 coefficients (C_4, C_6) and (C_{12}, C_{13}) . In the WZ channel, m_T^{WZ} provides the strongest constraining power, whilst the rapidity separation $|\Delta y_{Z,l_W}|$ yields a distinctly shaped contour compared to the other observables. This observable can thus be used to disentangle dimension-6 and dimension-8 effects. In the WW channel, the contours confirm the large impact of O_{10} .

We close by emphasising two important points. The first is the necessity of carrying out these studies at higher orders in perturbation theory. This is particularly relevant for the WW channel, where jet-veto effects are significant and resummation effects cannot be neglected. As a first step, NLO QCD corrections to the dimension-8 SMEFT contributions should be computed to validate the robustness of our findings. Secondly, we stress that the aim of our study is to examine dimension-8 effects whilst remaining agnostic about the UV origin of the operators we consider. Using particular UV models which can then be matched to the EFT is necessary to establish the hierarchy among the Wilson coefficients and the relative size of dimension-6 and dimension-8 effects.

Acknowledgements

The authors are grateful to Hao-Lin Li for providing the FeynRules implementation of the model in Ref. [54]. HF thanks Víctor Miralles for useful input on the fit procedure. We also thank Eugenia Celada, Gauthier Durieux, Ken Mimasu, Alejo Rossia, and Marion Thomas for helpful discussions. This work was supported by the European Research Council (ERC) under the European Union's Horizon 2020 research and innovation programme (Grant agreement No. 949451) and by a Royal Society University Research Fellowship through grant URF/R1/201553. HF acknowledges support from the European Union under the MSCA fellowship (Grant agreement No. 101208909).

A Additional results

In this section we present both marginalised and individual 95% CL bounds on the Wilson coefficient C_W at various cut-off scales Λ . In Tables 6 and 7 we show the results for WZ production. In Tables 8 and 9 we show the same for WW production.

References

- [1] ATLAS collaboration, Measurement of $W^{\pm}Z$ production cross sections and gauge boson polarisation in pp collisions at $\sqrt{s} = 13$ TeV with the ATLAS detector, Eur. Phys. J. C 79 (2019) 535 [1902.05759].
- [2] CMS collaboration, Measurement of the inclusive and differential WZ production cross sections, polarization angles, and triple gauge couplings in pp collisions at $\sqrt{s} = 13$ TeV, JHEP 07 (2022) 032 [2110.11231].
- [3] ATLAS collaboration, Observation of gauge boson joint-polarisation states in W±Z production from pp collisions at s=13 TeV with the ATLAS detector, Phys. Lett. B 843 (2023) 137895 [2211.09435].
- [4] M. Grazzini, S. Kallweit, S. Pozzorini, D. Rathlev and M. Wiesemann, W⁺W⁻ production at the LHC: fiducial cross sections and distributions in NNLO QCD, JHEP 08 (2016) 140 [1605.02716].
- [5] M. Grazzini, S. Kallweit, D. Rathlev and M. Wiesemann, $W^{\pm}Z$ production at the LHC: fiducial cross sections and distributions in NNLO QCD, JHEP **05** (2017) 139 [1703.09065].

obs	$C_W _{ \Lambda=3\mathrm{TeV}},\mathrm{marg}$	$C_W _{ \Lambda=4\mathrm{TeV}},\mathrm{marg}$	$C_W _{ \Lambda=5{ m TeV}}, { m marg}$
p_T^Z	[-1.90, 2.30]	[-3.02, 3.73]	[-4.57, 5.71]
p_T^W	[-2.11, 2.69]	[-3.33, 4.35]	[-5.04, 6.59]
m_T^{WZ}	[-1.73, 2.09]	[-2.52, 3.19]	[-3.69, 4.71]
$\Delta\Phi_{W\!,Z}$	[-6.45, 7.02]	_	_
$p_T^{ u}$	[-2.73, 3.40]	[-4.61, 5.80]	[-7.11, 9.00]
$ \Delta y_{Z,l_W} $	[-6.04, 6.28]	_	_
$\cos \theta_e^*$	[-4.88, 6.26]	_	_
p_T^Z	[-1.71, 2.26]	[-2.50, 3.47]	[-3.66, 5.16]
p_T^W	[-1.57, 2.09]	[-2.19, 3.11]	[-3.11, 4.59]
m_T^{WZ}	[-1.26, 1.57]	[-1.42, 1.97]	[-1.76, 2.59]
$\Delta\Phi_{W,Z}$	[-3.88, 4.23]	[-6.66, 7.28]	_
$p_T^ u$	[-2.47, 3.21]	[-4.00, 5.26]	[-6.04, 8.04]
$ \Delta y_{Z,l_W} $	[-3.52, 4.14]	[-6.04, 7.33]	_
$\cos \theta_e^*$	[-3.21, 4.47]	[-5.45, 7.71]	_

Table 6: Marginalised 95% CL bounds on the CP-even dimension-6 Wilson coefficient C_W from WZ production, shown per observable at NLO QCD. The results are presented for several cut-off scales Λ and are obtained by retaining terms up to $\mathcal{O}(\Lambda^{-4})$. The upper block corresponds to LHC results, whilst the lower block shows the HL-LHC projections.

- [6] B. Biedermann, M. Billoni, A. Denner, S. Dittmaier, L. Hofer, B. Jäger et al., Next-to-leading-order electroweak corrections to $pp \to W^+W^- \to 4$ leptons at the LHC, JHEP **06** (2016) 065 [1605.03419].
- [7] B. Biedermann, A. Denner, S. Dittmaier, L. Hofer and B. Jäger, *Electroweak corrections to* $pp \to \mu^+\mu^-e^+e^- + X$ at the LHC: a Higgs background study, *Phys. Rev. Lett.* **116** (2016) 161803 [1601.07787].
- [8] B. Biedermann, A. Denner and L. Hofer, Next-to-leading-order electroweak corrections to the production of three charged leptons plus missing energy at the LHC, JHEP 10 (2017) 043 [1708.06938].
- [9] M. Grazzini, S. Kallweit, J.M. Lindert, S. Pozzorini and M. Wiesemann, NNLO QCD + NLO EW with Matrix+OpenLoops: precise predictions for vector-boson pair production, JHEP 02 (2020) 087 [1912.00068].
- [10] D. Lombardi, M. Wiesemann and G. Zanderighi, W^+W^- production at NNLO+PS with $MINNLO_{PS}$, JHEP 11 (2021) 230 [2103.12077].
- [11] J.M. Lindert, D. Lombardi, M. Wiesemann, G. Zanderighi and S. Zanoli, WZ production at NNLO QCD and NLO EW matched to parton showers with MiNNLO_{PS}, JHEP 11 (2022) 036 [2208.12660].
- [12] M. Chiesa, C. Oleari and E. Re, NLO QCD+NLO EW corrections to diboson production

obs	$C_W _{ \Lambda=3\text{TeV}}$, ind	$C_W _{ \Lambda=4\text{TeV}}$, ind	$C_W _{ \Lambda=5\text{TeV}}$, ind
p_T^Z	[-1.61, 2.02]	[-2.87, 3.60]	[-4.48, 5.63]
p_T^W	[-1.76, 2.33]	[-3.14, 4.15]	[-4.91, 6.48]
m_T^{WZ}	[-1.26, 1.63]	[-2.25, 2.90]	[-3.51, 4.54]
$\Delta\Phi_{W\!,Z}$	[-6.33, 6.89]	_	_
$p_T^{ u}$	[-2.54, 3.21]	[-4.52, 5.71]	[-7.06, 8.93]
$ \Delta y_{Z,l_W} $	[-6.00, 6.29]	_	_
$\cos \theta_e^*$	[-4.73, 6.13]	_	_
p_T^Z	[-1.25, 1.79]	[-2.22, 3.19]	[-3.47, 4.98]
p_T^W	[-1.04, 1.57]	[-1.86, 2.80]	[-2.90, 4.38]
m_T^{WZ}	[-0.49, 0.79]	[-0.87, 1.41]	[-1.36, 2.20]
$\Delta\Phi_{W,Z}$	[-3.69, 4.02]	[-6.57, 7.15]	_
$p_T^ u$	[-2.12, 2.84]	[-3.78, 5.06]	[-5.90, 7.91]
$ \Delta y_{Z,l_W} $	[-3.33, 4.11]	[-5.93, 7.31]	_
$\cos \theta_e^*$	[-3.00, 4.27]	[-5.34, 7.59]	_

Table 7: Same as Table 6 but for individual bounds.

obs	$C_W _{ \Lambda=3\text{TeV}}, \text{ marg}$	$C_W _{ \Lambda=4\text{TeV}}, \text{ marg}$	$C_W _{ \Lambda=5\text{TeV}}, \text{ marg}$
$p_T^{l_{\mathrm{lead.}}}$	[-4.33, 4.54]	[-5.76, 6.11]	[-7.97, 8.54]
$p_T^{e\mu}$	[-4.09, 4.23]	[-6.14, 6.45]	[-9.09, 9.54]
$m_{e\mu}$	[-6.78, 7.04]	_	_
$p_T^{l_{\mathrm{lead.}}}$	[-3.59, 3.85]	[-3.85, 4.28]	[-4.33, 5.00]
$p_T^{e\mu}$	[-2.95, 3.19]	[-3.35, 3.80]	[-4.09, 4.80]
$m_{e\mu}$	[-4.09, 4.45]	[-6.19, 6.85]	[-8.02, 9.07]

Table 8: Same as Table 6 but for WW production.

 $matched\ to\ parton\ shower,\ Eur.\ Phys.\ J.\ C\ {\bf 80}\ (2020)\ 849\ [2005.12146].$

- [13] M. Grazzini, S. Kallweit, D. Rathlev and M. Wiesemann, Transverse-momentum resummation for vector-boson pair production at NNLL+NNLO, JHEP 08 (2015) 154 [1507.02565].
- [14] S. Kallweit, E. Re, L. Rottoli and M. Wiesemann, Accurate single- and double-differential resummation of colour-singlet processes with MATRIX+RADISH: W⁺W⁻ production at the LHC, JHEP 12 (2020) 147 [2004.07720].
- [15] J.M. Campbell, R.K. Ellis, T. Neumann and S. Seth, Transverse momentum resummation at $N^3LL+NNLO$ for diboson processes, JHEP **03** (2023) 080 [2210.10724].

obs	$C_W _{ \Lambda=3\text{TeV}}$, ind	$C_W _{ \Lambda=4\text{TeV}}$, ind	$C_W _{ \Lambda=5\text{TeV}}$, ind
$p_T^{l_{\mathrm{lead.}}}$	[-2.60, 2.81]	[-4.59, 4.96]	[-7.17, 7.76]
$p_T^{e\mu}$	[-3.13, 3.30]	[-5.57, 5.87]	[-8.71, 9.18]
$m_{e\mu}$	[-4.73, 5.00]	[-8.40, 8.89]	_
$p_T^{l_{\mathrm{lead.}}}$	[-0.95, 1.20]	[-1.70, 2.13]	[-2.66, 3.33]
$p_T^{e\mu}$	[-1.11, 1.37]	[-1.98, 2.44]	[-3.10, 3.82]
$m_{e\mu}$	[-2.34, 2.72]	[-4.17, 4.84]	[-6.51, 7.56]

Table 9: Same as Table 8 for individual bounds.

- [16] S. Dawson, P. Jaiswal, Y. Li, H. Ramani and M. Zeng, Resummation of jet veto logarithms at $N^3LL_a + NNLO$ for W^+W^- production at the LHC, Phys. Rev. D **94** (2016) 114014 [1606.01034].
- [17] J.M. Campbell, R.K. Ellis, T. Neumann and S. Seth, Jet-veto resummation at $N^3LL_p + NNLO$ in boson production processes, JHEP **04** (2023) 106 [2301.11768].
- [18] A. Gavardi, M.A. Lim, S. Alioli and F.J. Tackmann, NNLO+PS W⁺ W⁻ production using jet veto resummation at NNLL', JHEP 12 (2023) 069 [2308.11577].
- [19] R.G. Stuart, Gauge invariance, analyticity and physical observables at the Z0 resonance, Phys. Lett. B 262 (1991) 113.
- [20] A. Aeppli, F. Cuypers and G.J. van Oldenborgh, O(Gamma) corrections to W pair production in e+ e- and gamma gamma collisions, Phys. Lett. B 314 (1993) 413 [hep-ph/9303236].
- [21] A. Aeppli, G.J. van Oldenborgh and D. Wyler, Unstable particles in one loop calculations, Nucl. Phys. B 428 (1994) 126 [hep-ph/9312212].
- [22] A. Denner, S. Dittmaier, M. Roth and D. Wackeroth, Electroweak radiative corrections to e+ e- —> W W —> 4 fermions in double pole approximation: The RACOONWW approach, Nucl. Phys. B 587 (2000) 67 [hep-ph/0006307].
- [23] P. Richardson, Spin correlations in Monte Carlo simulations, JHEP 11 (2001) 029 [hep-ph/0110108].
- [24] C.F. Uhlemann and N. Kauer, Narrow-width approximation accuracy, Nucl. Phys. B 814 (2009) 195 [0807.4112].
- [25] P. Artoisenet, R. Frederix, O. Mattelaer and R. Rietkerk, *Automatic spin-entangled decays of heavy resonances in Monte Carlo simulations*, *JHEP* **03** (2013) 015 [1212.3460].
- [26] A. Denner and G. Pelliccioli, Polarized electroweak bosons in W⁺W⁻ production at the LHC including NLO QCD effects, JHEP **09** (2020) 164 [2006.14867].
- [27] A. Denner and G. Pelliccioli, NLO QCD predictions for doubly-polarized WZ production at the LHC, Phys. Lett. B 814 (2021) 136107 [2010.07149].
- [28] R. Poncelet and A. Popescu, NNLO QCD study of polarised W^+W^- production at the LHC, JHEP 07 (2021) 023 [2102.13583].

- [29] D.N. Le and J. Baglio, Doubly-polarized WZ hadronic cross sections at NLO QCD + EW accuracy, Eur. Phys. J. C 82 (2022) 917 [2203.01470].
- [30] D.N. Le, J. Baglio and T.N. Dao, Doubly-polarized WZ hadronic production at NLO QCD+EW: calculation method and further results, Eur. Phys. J. C 82 (2022) 1103 [2208.09232].
- [31] A. Denner, C. Haitz and G. Pelliccioli, NLO EW corrections to polarised W+W- production and decay at the LHC, Phys. Lett. B 850 (2024) 138539 [2311.16031].
- [32] T.N. Dao and D.N. Le, Enhancing the doubly-longitudinal polarization in WZ production at the LHC, Commun. in Phys. 33 (2023) 223 [2302.03324].
- [33] M. Hoppe, M. Schönherr and F. Siegert, *Polarised cross sections for vector boson production with Sherpa*, *JHEP* **04** (2024) 001 [2310.14803].
- [34] G. Pelliccioli and G. Zanderighi, *Polarised-boson pairs at the LHC with NLOPS accuracy*, Eur. Phys. J. C 84 (2024) 16 [2311.05220].
- [35] M. Rubin, G.P. Salam and S. Sapeta, Giant QCD K-factors beyond NLO, JHEP 09 (2010) 084 [1006.2144].
- [36] A. Denner and S. Pozzorini, One loop leading logarithms in electroweak radiative corrections.

 1. Results, Eur. Phys. J. C 18 (2001) 461 [hep-ph/0010201].
- [37] E. Accomando, A. Denner and A. Kaiser, Logarithmic electroweak corrections to gauge-boson pair production at the LHC, Nucl. Phys. B 706 (2005) 325 [hep-ph/0409247].
- [38] A. Falkowski, M. Gonzalez-Alonso, A. Greljo and D. Marzocca, Global constraints on anomalous triple gauge couplings in effective field theory approach, Phys. Rev. Lett. 116 (2016) 011801 [1508.00581].
- [39] A. Falkowski, M. Gonzalez-Alonso, A. Greljo, D. Marzocca and M. Son, *Anomalous Triple Gauge Couplings in the Effective Field Theory Approach at the LHC*, *JHEP* **02** (2017) 115 [1609.06312].
- [40] A. Helset and M. Trott, On interference and non-interference in the SMEFT, JHEP 04 (2018) 038 [1711.07954].
- [41] J. Baglio, S. Dawson and I.M. Lewis, An NLO QCD effective field theory analysis of W⁺W⁻ production at the LHC including fermionic operators, Phys. Rev. D **96** (2017) 073003 [1708.03332].
- [42] A. Azatov, J. Elias-Miro, Y. Reyimuaji and E. Venturini, *Novel measurements of anomalous triple gauge couplings for the LHC*, *JHEP* **10** (2017) 027 [1707.08060].
- [43] R. Franceschini, G. Panico, A. Pomarol, F. Riva and A. Wulzer, Electroweak Precision Tests in High-Energy Diboson Processes, JHEP 02 (2018) 111 [1712.01310].
- [44] M. Chiesa, A. Denner and J.-N. Lang, Anomalous triple-gauge-boson interactions in vector-boson pair production with RECOLA2, Eur. Phys. J. C 78 (2018) 467 [1804.01477].
- [45] J. Baglio, S. Dawson and I.M. Lewis, NLO effects in EFT fits to W⁺W⁻ production at the LHC, Phys. Rev. D 99 (2019) 035029 [1812.00214].
- [46] D. Liu and L.-T. Wang, Prospects for precision measurement of diboson processes in the semileptonic decay channel in future LHC runs, Phys. Rev. D 99 (2019) 055001 [1804.08688].

- [47] C. Grojean, M. Montull and M. Riembau, Diboson at the LHC vs LEP, JHEP 03 (2019) 020 [1810.05149].
- [48] A. Azatov, D. Barducci and E. Venturini, *Precision diboson measurements at hadron colliders*, *JHEP* **04** (2019) 075 [1901.04821].
- [49] J. Baglio, S. Dawson and S. Homiller, QCD corrections in Standard Model EFT fits to WZ and WW production, Phys. Rev. D 100 (2019) 113010 [1909.11576].
- [50] J. Baglio, S. Dawson, S. Homiller, S.D. Lane and I.M. Lewis, Validity of standard model EFT studies of VH and VV production at NLO, Phys. Rev. D 101 (2020) 115004 [2003.07862].
- [51] J. Ellis, M. Madigan, K. Mimasu, V. Sanz and T. You, Top, Higgs, Diboson and Electroweak Fit to the Standard Model Effective Field Theory, JHEP **04** (2021) 279 [2012.02779].
- [52] C. Degrande and J. Touchèque, A reduced basis for CP violation in SMEFT at colliders and its application to diboson production, JHEP 04 (2022) 032 [2110.02993].
- [53] A. Rossia, M. Thomas and E. Vryonidou, Diboson production in the SMEFT from gluon fusion, JHEP 11 (2023) 132 [2306.09963].
- [54] C. Degrande and H.-L. Li, Impact of dimension-8 SMEFT operators on diboson productions, JHEP 06 (2023) 149 [2303.10493].
- [55] R. Aoude, E. Madge, F. Maltoni and L. Mantani, Probing new physics through entanglement in diboson production, JHEP 12 (2023) 017 [2307.09675].
- [56] C. Degrande and M. Maltoni, EFT observable stability under NLO corrections through interference revival, Phys. Lett. B 856 (2024) 138970 [2403.16894].
- [57] H. El Faham, G. Pelliccioli and E. Vryonidou, Triple-gauge couplings in LHC diboson production: a SMEFT view from every angle, JHEP 08 (2024) 087 [2405.19083].
- [58] M.O.A. Thomas and E. Vryonidou, CP violation in loop-induced diboson production, JHEP 03 (2025) 038 [2411.00959].
- [59] U. Haisch, J. Linder, G. Pelliccioli, E. Re and G. Zanderighi, Polarized-boson pairs at NLO in the SMEFT, 2507.21768.
- [60] G. Panico, F. Riva and A. Wulzer, Diboson interference resurrection, Phys. Lett. B 776 (2018) 473 [1708.07823].
- [61] L. Mantani and V. Sanz, Probing the flavour-blind SMEFT: EFT validity and the interplay of energy scales, JHEP 06 (2025) 147 [2503.02935].
- [62] J. Ellis, H.-J. He and R.-Q. Xiao, Probing neutral triple gauge couplings at the LHC and future hadron colliders, Phys. Rev. D 107 (2023) 035005 [2206.11676].
- [63] T. Corbett, J. Desai, O.J.P. Éboli, M.C. Gonzalez-Garcia, M. Martines and P. Reimitz, Impact of dimension-eight SMEFT operators in the electroweak precision observables and triple gauge couplings analysis in universal SMEFT, Phys. Rev. D 107 (2023) 115013 [2304.03305].
- [64] J. Ellis, K. Mimasu and F. Zampedri, Dimension-8 SMEFT analysis of minimal scalar field extensions of the Standard Model, JHEP 10 (2023) 051 [2304.06663].
- [65] J. Ellis, S.-F. Ge and K. Ma, Hadron collider probes of the quartic couplings of gluons to the photon and Z boson, JHEP **04** (2022) 123 [2112.06729].

- [66] A. Martin, A case study of SMEFT $\mathcal{O}\left(1/\Lambda^4\right)$ effects in diboson processes: $pp \to W(\ell\nu)\gamma$, JHEP **05** (2024) 223 [2312.09867].
- [67] J. Bellm, S. Gieseke, N. Greiner, G. Heinrich, S. Plätzer, C. Reuschle et al., Anomalous coupling, top-mass and parton-shower effects in W⁺W⁻ production, JHEP **05** (2016) 106 [1602.05141].
- [68] D. Gillies, A. Banfi, A. Martin and M.A. Lim, Dimension-8 operators in W⁺W⁻ production via gluon fusion, JHEP **06** (2025) 111 [2412.16020].
- [69] B. Grzadkowski, M. Iskrzynski, M. Misiak and J. Rosiek, Dimension-Six Terms in the Standard Model Lagrangian, JHEP 10 (2010) 085 [1008.4884].
- [70] H.-L. Li, Z. Ren, J. Shu, M.-L. Xiao, J.-H. Yu and Y.-H. Zheng, Complete set of dimension-eight operators in the standard model effective field theory, Phys. Rev. D 104 (2021) 015026 [2005.00008].
- [71] C.W. Murphy, Dimension-8 operators in the Standard Model Effective Field Theory, JHEP 10 (2020) 174 [2005.00059].
- [72] H.-L. Li, Z. Ren, M.-L. Xiao, J.-H. Yu and Y.-H. Zheng, Operators for generic effective field theory at any dimension: on-shell amplitude basis construction, JHEP **04** (2022) 140 [2201.04639].
- [73] R.V. Harlander, T. Kempkens and M.C. Schaaf, Standard model effective field theory up to mass dimension 12, Phys. Rev. D 108 (2023) 055020 [2305.06832].
- [74] R.V. Harlander and M.C. Schaaf, AutoEFT: Automated operator construction for effective field theories, Comput. Phys. Commun. 300 (2024) 109198 [2309.15783].
- [75] E. Celada, T. Giani, J. ter Hoeve, L. Mantani, J. Rojo, A.N. Rossia et al., Mapping the SMEFT at high-energy colliders: from LEP and the (HL-)LHC to the FCC-ee, JHEP 09 (2024) 091 [2404.12809].
- [76] G. D'Ambrosio, G.F. Giudice, G. Isidori and A. Strumia, *Minimal flavor violation: An Effective field theory approach*, *Nucl. Phys. B* **645** (2002) 155 [hep-ph/0207036].
- [77] S. Dittmaier and M. Krämer, Electroweak radiative corrections to W boson production at hadron colliders, Phys. Rev. D 65 (2002) 073007 [hep-ph/0109062].
- [78] I. Brivio, S. Dawson, J. de Blas, G. Durieux, P. Savard, A. Denner et al., *Electroweak input parameters*, 2111.12515.
- [79] A. Denner, S. Dittmaier, M. Roth and L.H. Wieders, Electroweak corrections to charged-current e+ e- —> 4 fermion processes: Technical details and further results, Nucl. Phys. B 724 (2005) 247 [hep-ph/0505042].
- [80] A. Denner and S. Dittmaier, The Complex-mass scheme for perturbative calculations with unstable particles, Nucl. Phys. B Proc. Suppl. 160 (2006) 22 [hep-ph/0605312].
- [81] A. Denner and S. Dittmaier, Electroweak Radiative Corrections for Collider Physics, Phys. Rept. 864 (2020) 1 [1912.06823].
- [82] NNPDF collaboration, Parton distributions from high-precision collider data, Eur. Phys. J. C 77 (2017) 663 [1706.00428].
- [83] A. Buckley, J. Ferrando, S. Lloyd, K. Nordström, B. Page, M. Rüfenacht et al., LHAPDF6: parton density access in the LHC precision era, Eur. Phys. J. C 75 (2015) 132 [1412.7420].

- [84] C. Degrande, G. Durieux, F. Maltoni, K. Mimasu, E. Vryonidou and C. Zhang, Automated one-loop computations in the standard model effective field theory, Phys. Rev. D 103 (2021) 096024 [2008.11743].
- [85] J. Alwall, R. Frederix, S. Frixione, V. Hirschi, F. Maltoni, O. Mattelaer et al., The automated computation of tree-level and next-to-leading order differential cross sections, and their matching to parton shower simulations, JHEP 07 (2014) 079 [1405.0301].
- [86] C. Degrande, C. Duhr, B. Fuks, D. Grellscheid, O. Mattelaer and T. Reiter, UFO The Universal FeynRules Output, Comput. Phys. Commun. 183 (2012) 1201 [1108.2040].
- [87] A. Alloul, N.D. Christensen, C. Degrande, C. Duhr and B. Fuks, FeynRules 2.0 A complete toolbox for tree-level phenomenology, Comput. Phys. Commun. 185 (2014) 2250 [1310.1921].
- [88] ATLAS collaboration, Measurement of fiducial and differential W^+W^- production cross-sections at $\sqrt{s}=13$ TeV with the ATLAS detector, Eur. Phys. J. C **79** (2019) 884 [1905.04242].
- [89] F. Boudjema and R.K. Singh, A Model independent spin analysis of fundamental particles using azimuthal asymmetries, JHEP 07 (2009) 028 [0903.4705].
- [90] W.J. Stirling and E. Vryonidou, *Electroweak gauge boson polarisation at the LHC*, *JHEP* **07** (2012) 124 [1204.6427].
- [91] A. Ballestrero, E. Maina and G. Pelliccioli, W boson polarization in vector boson scattering at the LHC, JHEP 03 (2018) 170 [1710.09339].
- [92] E. Maguire, L. Heinrich and G. Watt, HEPData: a repository for high energy physics data, J. Phys. Conf. Ser. 898 (2017) 102006 [1704.05473].
- [93] R. Contino, A. Falkowski, F. Goertz, C. Grojean and F. Riva, On the Validity of the Effective Field Theory Approach to SM Precision Tests, JHEP 07 (2016) 144 [1604.06444].
- [94] D. Liu, A. Pomarol, R. Rattazzi and F. Riva, Patterns of Strong Coupling for LHC Searches, JHEP 11 (2016) 141 [1603.03064].